The Astrophysical Journal, 869:69 (19pp), 2018 December 10 https://doi.org/10.3847/1538-4357/aaed26

Successive Flux Rope Eruptions from δ-sunspots Region of NOAA 12673 and Associated X-class Eruptive Flares on 2017 September 6

Prabir K. Mitra[1], Bhuwan Joshi[1], Avijeet Prasad[1], Astrid M. Veronig[2], and R. Bhattacharyya[1]
[1] Udaipur Solar Observatory, Physical Research Laboratory, Udaipur 313 001, India; prabir@prl.res.in
[2] Institute of Physics & Kanzelhöhe Observatory, University of Graz, Universitätsplatz 5, A-8010 Graz, Austria
Received 2018 June 11; revised 2018 October 27; accepted 2018 October 29; published 2018 December 13

Abstract

In this article, we present a multiwavelength analysis of two X-class solar eruptive flares of classes X2.2 and X9.3 that occurred in the sigmoidal active region NOAA 12673 on 2017 September 6, by combining observations of Atmospheric Imaging Assembly and Helioseismic Magnetic Imager instruments on board the *Solar Dynamics Observatory*. On the day of the reported activity, the photospheric structure of the active region displayed a very complex network of δ-sunspots that gave rise to the formation of a coronal sigmoid observed in the hot extreme-ultraviolet channels. Both X-class flares initiated from the core of the sigmoid sequentially within an interval of $\sim$3 hr and progressed as a single sigmoid-to-arcade event. Differential emission measure analysis reveals strong heating of plasma at the core of the active region right from the preflare phase, which further intensified and spatially expanded during each event. The identification of a preexisting magnetic null by non-force-free-field modeling of the coronal magnetic fields at the location of early flare brightenings and remote faint ribbon-like structures during the preflare phase, which were magnetically connected with the core region, provide support for the breakout model of solar eruption. The magnetic extrapolations also reveal flux rope structures before both flares, which are subsequently supported by the observations of the eruption of hot extreme-ultraviolet channels. The second X-class flare diverged from the standard flare scenario in the evolution of two sets of flare ribbons, which are spatially well separated, providing firm evidence of magnetic reconnections at two coronal heights.

Key words: Sun: activity – Sun: corona – Sun: filaments, prominences – Sun: flares

Supporting material: animation

1. Introduction

Solar eruptive flares and associated coronal mass ejections (CMEs) produce large-scale changes in coronal magnetic field configurations. The magnetic and plasma structures of Earth-directed CMEs have been regularly recorded by in situ measurements at 1 au, and these are known to drive hazardous effects at the near-Earth environment. Probing the exact magnetic configuration of flare-producing active regions (ARs) during the preeruption phase and their role in driving the subsequent eruptive phenomena has been among the major objectives of contemporary research in solar physics.

The standard flare model, also known as the CSHKP model (Carmichael 1964; Sturrock 1966; Hirayama 1974; Kopp & Pneuman 1976), recognizes that the initiation of a solar eruptive flare is intrinsically related to the dynamic activation of a filament (or prominence) by some kind of instability in the system. Once the filament attains eruptive motions, large-scale magnetic reconnection sets in underneath it in a vertical current sheet that accelerates the particles to relativistic speeds and heats the plasma to million Kelvin (MK) temperatures. It is generally accepted that the energy source for the observed eruptive phenomena is derived from the free energy contained in sheared or twisted magnetic fields (Forbes 2000). Although the standard flare model takes into account most of the commonly observed phenomena, such as flare ribbons, looptop and footpoint sources, cusp structure following the passage of the filament, postflare loop arcade, and so forth (e.g., see review by Fletcher et al. 2011; Benz 2017), it remains silent regarding the mechanism that triggers the filament eruption in the first place. We should also note that, despite the general applicability of the standard flare model, many CME/eruptive flares exhibit features that deviate from this scenario (e.g., see Joshi et al. 2012).

From a theoretical point of view, the structure of an erupting filament or filament channel is attributed to a magnetic flux rope (e.g., see Gibson & Fan 2006), whose exact topology and formation process remain unclear and debatable. There are two basic classes of models that describe the magnetic configuration of the system initially: sheared arcade and twisted flux rope. A sheared magnetic arcade extends along the polarity inversion line (PIL), whereas the flux rope is thought to lie above the inversion line. Considering these initial configurations, the onset of eruption can be attributed to either loss of equilibrium/ideal instability or magnetic reconnection (see reviews by Klimchuk 2001; Forbes et al. 2006; Vršnak 2008; Chen 2011; Green et al. 2018). In general, the preexistence of the flux rope is a prerequisite for ideal models. On the other hand, reconnection models can work with either a sheared arcade or a twisted flux rope. In observations, the coronal sigmoid (e.g., see Manoharan et al. 1996; Hudson et al. 1998) and/or erupting hot extreme-ultraviolet (EUV) channels (e.g., see Patsourakos et al. 2013; Cheng & Ding 2016) are thought to provide strong support toward the flux rope scenario. Thorough multiwavelength case studies of major solar eruptions are extremely useful to probe whether the flux rope signatures preexist or develop on the fly during the pre- or early phases of solar flares.

To illustrate the eruptive flares in complex ARs, we divide the underlying magnetic configuration in two parts: core and envelope fields (Moore et al. 2001). Core fields denote the low-lying magnetic flux system, close to the PIL, and it is assumed that a major part of the stored magnetic energy lies in this region. The envelope refers to the outer large-scale overlying flux system. For a successful eruption, the stressed core field must destabilize and eventually erupt through the barrier of the overlying flux system to generate a CME. Two representative models of solar eruptions—tether-cutting and breakout—rely on the magnetic reconnection before the flare (and/or CME onset) that trigger the eruption of the core fields. However, the early reconnection proceeds quite differently in the two models. The preflare configuration in the tether-cutting model comprises a single, highly sheared, bipolar AR, with the earliest reconnection (i.e., triggering process) taking place deep in the sheared core fields (Moore & Roumeliotis 1992; Moore et al. 2001). On the other hand, the breakout model involves a multipolar topology, containing one or more preexisting coronal null points. In this case, the CME onset is triggered by reconnection occurring well above the core region (Antiochos et al. 1999). The basic reconnection conditions for both models give rise to differences in the sequence and location of the preflare brightenings. In the tether-cutting model, all preflare activity resides beneath the flare reconnection site. In contrast, the breakout model causes both core and remote brightenings before flare/CME initiation (e.g., see Sterling & Moore 2001). A thorough investigation of the sites of preflare brightenings with respect to the location of flux rope/filament along with coronal null points is essential to understand the triggering process of solar eruptions. However, after the successful trigger, once the flux rope attains eruptive expansion, the standard flare reconnection occurs in a vertical current sheet that is formed underneath the flux rope, and this scenario is common to all the models of eruptive flares (e.g., see Veronig et al. 2006; Liu et al. 2008; Joshi et al. 2013, 2016).

In this article, we present comprehensive multiwavelength analysis of two major solar eruptive flares of classes X2.2 and X9.3 that occurred on 2017 September 6 in the AR NOAA 12673. Interestingly, the two flares initiated from the same location of the sigmoidal AR and occurred within an interval of ~3 hr. We investigate the processes associated with flare initiation and subsequent eruption by utilizing multichannel high-resolution observations from the Atmospheric Imaging Assembly (AIA; Lemen et al. 2012) on board the *Solar Dynamics Observatory* (*SDO*; Pesnell et al. 2012). In particular, the study of the distribution of hot plasma within the sigmoid at various phases by differential emission measure (DEM) technique provide important insights about the plasma heating caused by energy deposition by accelerated particles. We have further undertaken a comprehensive study of the photospheric magnetic structures thanks to high-resolution line-of-sight (LOS) magnetograms from the Helioseismic and Magnetic Imager (HMI; Schou et al. 2012). Furthermore, we use the photospheric vector magnetograms from HMI as an input to a non-force-free-field (NFFF) magnetic field extrapolation model (Hu et al. 2008). Such extrapolations have been recently used to successfully model the magnetohydrodynamic evolution of flaring ARs (see Prasad et al. 2018). Multiwavelength analysis in combination with coronal magnetic field modeling has clarified important aspects of solar eruptions, such as triggering of flux rope eruption and its early evolution in the low corona, which are examined in terms of scope and limitations of the standard flare model. Section 2 provides a brief account of the observational data and analysis techniques. In Section 3, we present multiwavelength analysis and derive the observational results on the basis of comprehensive measurements taken at photospheric, chromospheric, and coronal levels. In Section 4, we compare the chromospheric and coronal observations of different flare associated features with magnetic topology and configurations obtained with NFFF modeling of the AR corona. We discuss and interpret our results in Section 5.

2. Observations and Data Analysis Techniques

In this article, we use observational data from the AIA (Lemen et al. 2012) and the HMI (Schou et al. 2012) on board the *SDO* (Pesnell et al. 2012). AIA observes the Sun in seven EUV filters (94 Å, 131 Å, 171 Å, 193 Å, 211 Å, 304 Å, and 335 Å), two ultraviolet (UV) filters (1600 Å and 1700 Å), and one white light filter (4500 Å). AIA produces 4096 × 4096 pixel full-disk solar images at a spatial resolution of 0.″6 pixel^{-1} and temporal cadence of 12 s for EUV filters, 24 s for UV filters, and 3600 s for the white light filter.

DEM analysis provides insights of multithermal processes associated with energy release in solar eruptive phenomena. Observations from the six coronal EUV filters of AIA (94 Å, 131 Å, 171 Å, 193 Å, 211 Å, and 335 Å) are used for computation of DEM. A brief account of the theoretical background for DEM along with its analysis technique is given in Section 3.4.

For studying the photospheric structures associated with the AR NOAA 12673, we have used HMI intensity and LOS magnetogram images. HMI produces full-disk LOS intensity (continuum) and magnetogram images of 4096 × 4096 pixels at a spatial resolution of 0.″5 pixel^{-1} and 45 s temporal cadence. To have exact spatial alignment between AIA and HMI images, we have processed the HMI images by use of the SSW routine hmi_prep.pro, which converts spatial resolution of HMI images from 0.″5 pixel^{-1} to 0.″6 pixel^{-1} and resolves the ~180° roll angle of level 1 images.

Coronal magnetic field lines are extrapolated by using the hmi.sharp_cea_720s series from *SDO*/HMI, which takes full-disk vector magnetograms at a spatial resolution of 0.″5 pixel^{-1} and temporal cadence of 720 s. The magnetograms in this data set are first remapped on to a Lambert cylindrical equal-area projection and then are transformed into the heliographic coordinates (Gary & Hagyard 1990), which is essential for extrapolations in Cartesian geometry. In this case, the magnetogram represents a cutout image of the AR of dimensions 688 × 448 pixels, which corresponds to a physical size of ~250 and ~160 Mm, respectively, on the Sun. Extrapolations were done up to an extent of 448 pixels vertically, which translates to a height of ~160 Mm from the photosphere. For visualizing the modeled field lines, we have used Visualization and Analysis Platform for Ocean, Atmosphere, and Solar Researchers (VAPOR[3]; Clyne et al. 2007) software, which produces an interactive 3D visualization environment.

CMEs associated with the X-class flares were observed by the C2 and C3 of the Large Angle and Spectrometric Coronagraph (LASCO; Brueckner et al. 1995) on board the

[3] https://www.vapor.ucar.edu/

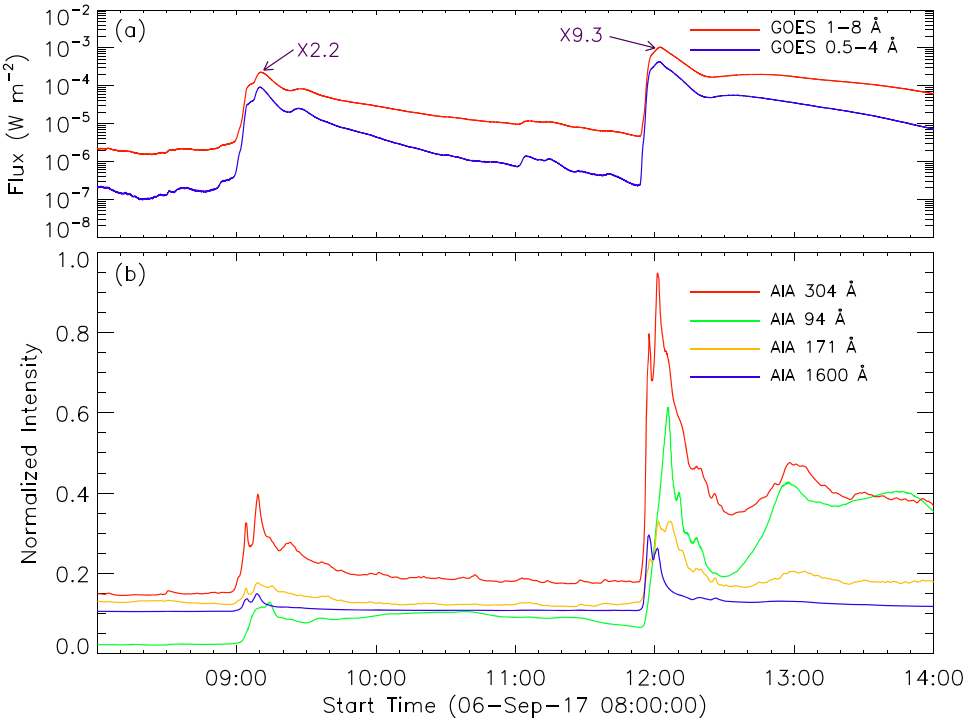

Figure 1. Panel (a): *GOES* X-ray flux profiles in 1–8 Å and 0.5–4 Å from 08:00 UT to 14:00 UT on 2017 September 6, showing the occurrence of two X-class flares of intensities X2.2 and X9.3, respectively. Panel (b): AIA light curves normalized by the peak intensity of the respective AIA filters. For clear visualization, the AIA light curves have been scaled by factors of 1, 0.65, 0.33, and 0.33 for 304 Å, 94 Å, 171 Å, and 1600 Å channels, respectively. (An animation displaying the morphologic evolution of the AR from 08:00 UT to 14:00 UT in AIA 94 Å and 304 Å channels with time variation of *GOES* SXR flux is available in the HTML (online) version of the article.)

(An animation of this figure is available.)

Table 1
Summary of the Two X-class Flares Occurring on 2017 September 6

Sr. No.	Flare Class	Time Start	Time Peak	Time End	Location of the Center of the Sigmoid
1	X2.2	08:59 UT	09:10 UT	09:36 UT	$(x, y) \approx (510'', -230'')$
2	X9.3	11:53 UT	12:02 UT	13:09 UT	$(x, y) \approx (530'', -250'')$

Solar and Heliospheric Observatory (Domingo et al. 1995). C2 and C3 are white light coronagraphs imaging from 1.5 to 6 $R_\odot$ and from 3.7 to 30 $R_\odot$, respectively.

3. Multiwavelength Analysis and Results

3.1. Event Overview

The investigation performed in this article corresponds to the observation of the AR NOAA 12673 on 2017 September 6 from 08:00 UT to 14:00 UT. In this period, the AR produced two X-class flares, both associated with CME. In Figure 1, we compare the soft X-ray (SXR) light curves from *GOES* (Figure 1(a)) with (E)UV time profiles from AIA (Figure 1(b)). Light curves at all the energies suggest the occurrence of the impulsive phase of the first flare (X2.2) at ∼09:00–09:10 UT. After ∼09:16 UT, the X-ray flux of either channels slowly decreased up to ∼11:55 UT and thereafter rapidly increased, indicating the sudden initiation of the second flare (X9.3). The abrupt increase in X-ray flux is accompanied by rapid build up of (E)UV emission. After ∼12:00 UT, the X-ray flux underwent fast decay until ∼12:22 UT, which was followed by an extended phase during which the flux initially increased and then decreased very gradually. Notably, this two-step evolution of the second flare's decay phase is more prominent in the EUV light curves (see Figures 1(a) and (b)). A summary of these two X-class flares is given in Table 1.

According to the Solar Eruptive Event Detection System (SEEDS) CME catalog,[4] both X-class flares were associated with CMEs. The CME corresponding to the X2.2 flare was detected at 11:00 UT at 5.02 $R_\odot$ (half-max lead). This relatively narrow CME (angular width 44°) was traveling along PA of 255° with linear fit speed 279 km s^{-1} in the field of view of LASCO C2 (top panels of Figure 2). The CME corresponding to the X9.3 flare was detected at 12:36 UT at 3.50 $R_\odot$ (half-max lead), which had an angular width of 145° and linear fit speed of 505 km s^{-1} along PA 241° (bottom panels of Figure 2).

3.2. X2.2 Flare

3.2.1. Flare Evolution

Figure 3 displays a series of AIA 94 Å (panels (a)–(f)) and AIA 304 Å (panels (g)–(l)) images showing the time evolution of the X2.2 flare. The overall activity site appeared to form an inverted S-shaped extended region in the corona (i.e., a coronal

[4] http://spaceweather.gmu.edu/seeds/monthly.php?a=2017&b=09

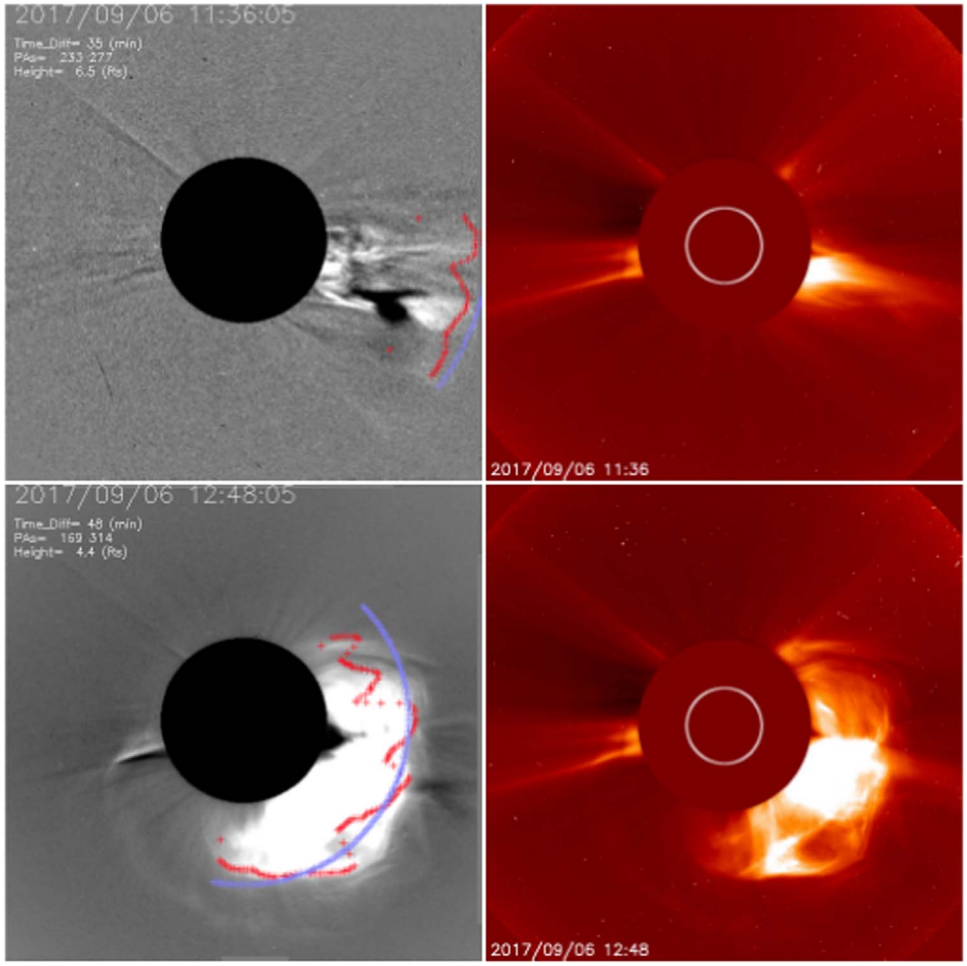

Figure 2. Top panels: running difference (left) and direct (right) images obtained from LASCO C2 coronagraph showing the CME associated with the X2.2 flare. Bottom panels: running difference (left) and direct (right) images obtained from LASCO C2 coronagraph showing the CME associated with the X9.3 flare. The blue and red lines on the difference images indicate the approximate position of the leading edge created by using two different techniques.

sigmoid) (Manoharan et al. 1996; Rust & Kumar 1996). As expected, this sigmoidal structure was most prominent and distinct during the preflare stages (indicated by black dotted curved lines in Figures 3(b) and (h)). Although we noticed a few compact and short-lived structures in the sigmoidal region, they did not seem to contribute much toward the overall brightness variation in the preflare phase. The only standout and consistent feature, observed from long before the initiation of the flare, was a small loop, which is shown in the box in Figure 3(b). Flare initiation occurred at ∼09:00 UT when this loop-like structure started broadening. This was followed by the activation of a filament in the middle of the sigmoid shaped in the form of a question mark ("?") notation (see Figure 3(c)). This filament emitted intensely during the peak phase of the flare (Figures 3(c)–(d) and in the respective zoomed cutouts). The comparison of spatial distribution of the filament with photospheric magnetic contours reveals the filament to lie over the photospheric PIL (the PIL has been indicated by the tiny blue arrows in the cutout of Figure 3(c)). The filament activation ceased at ∼09:15 UT, and the flare emission started to decline thereafter. Although the activated filament did not show any further evolution in the corona following the flare maximum, the signatures of plasma eruption are simultaneously noted from the overlying coronal environment (marked by white arrows in Figure 3(e)). The eruption scenario is further discussed in Section 3.2.2.

The observation in AIA 304 Å reveals some interesting aspects of energy release processes in chromospheric layer. A very localized bright spot can be found in AIA 304 Å images before the flare (indicated by an arrow in Figure 3(h)). We recall the emergence of a bright compact loop structure in AIA 94 Å images (region inside the box in Figure 3(b)) before the X2.2 flare at the same region (see Figures 3(b) and (h)). This spatial and temporal correlation between coronal and chromospheric activities suggests a magnetic coupling between the chromospheric and coronal layers during small-scale preflare processes. The peak phase of the flare in AIA 304 Å emission is characterized by two distinct peaks at ∼09:04 UT and ∼09:09 UT (see Figure 1(b)). The corresponding images (Figures 3(i)–(j)) clearly show intense emission from regions close to the activated filament, whereas the ribbon structures remain short and not so well separated during the maximum phase (Figures 3(i) and (j)) and beyond. AIA 304 Å images reveal a bright, closed loop-like structure in the decay phase, at the middle of the sigmoid (Figure 3(l)), which possibly resulted from cooling of a hot loop observed in the AIA 94 Å filter during early flare stages (Figures 3(c)–(d)).

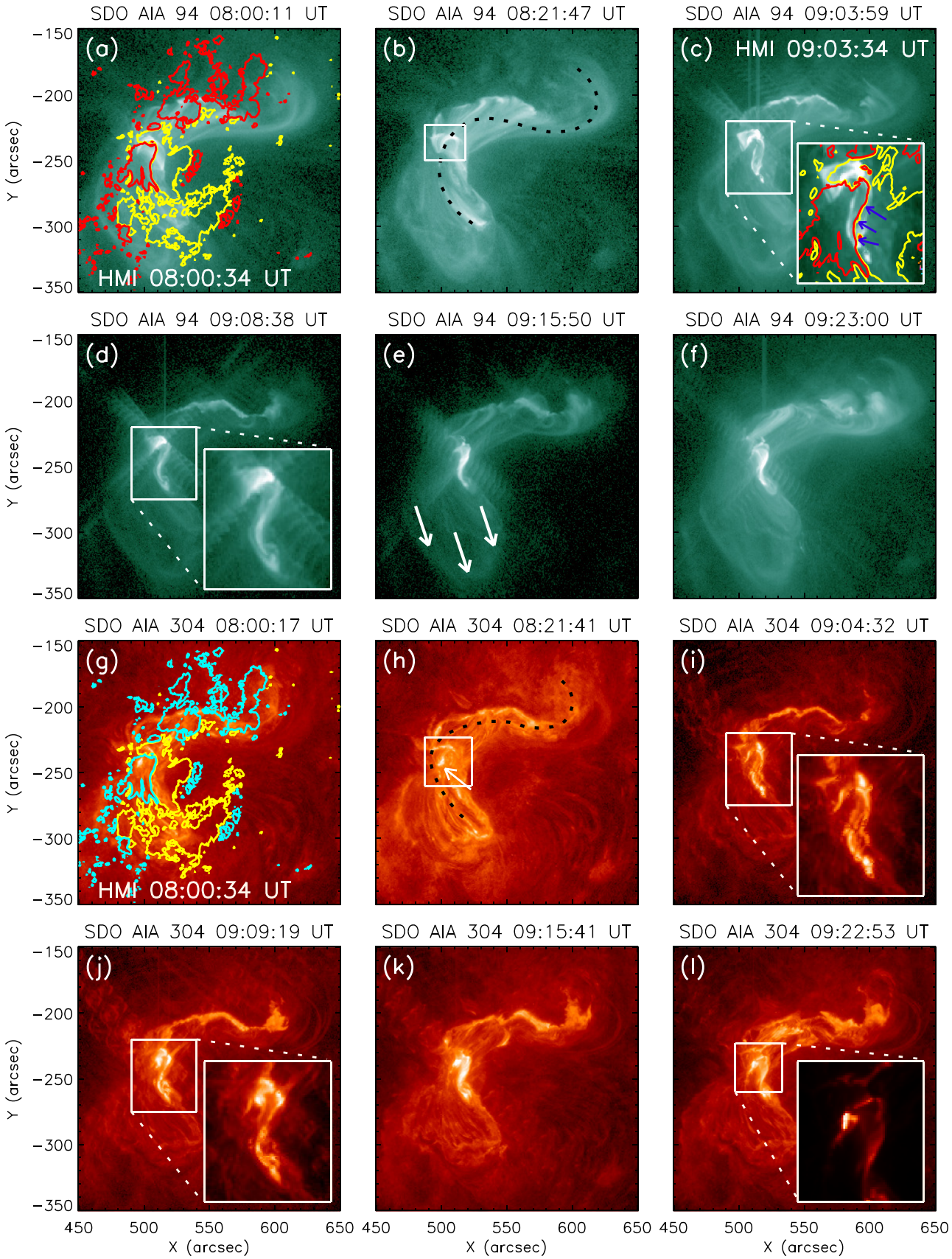

Figure 3. Sequence of AIA 94 Å images (panels (a)–(f)) and AIA 304 Å images (panels (g)–(l)) showing the morphological evolution of the X2.2 flare. Insets in panels (c), (d), (i), (j), and (l) show zoomed-in images of the selected regions shown in smaller boxes in the corresponding panels. Contours of HMI LOS magnetograms are overplotted on selected AIA images (in panels (a), (c), and (g)) at levels of ±250 G. Yellow contours refer to positive polarity, whereas red and blue contours refer to negative polarity.

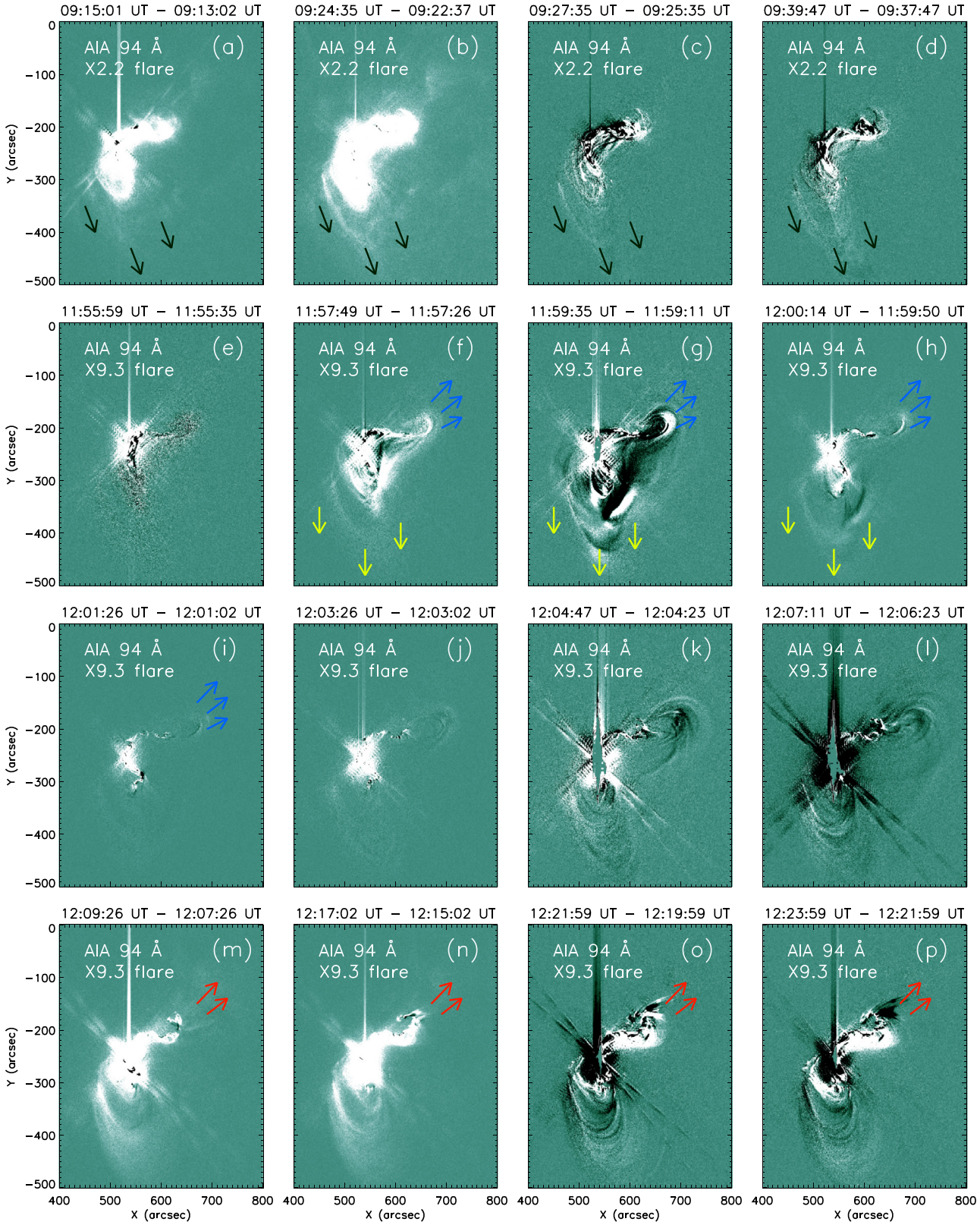

Figure 4. Sequence of AIA 94 Å running difference images showing different phases and directions of plasma eruption from the AR during the X2.2 (panels (a)–(d)) and the X9.3 (panels (e)–(p)) flares. Arrows in different panels indicate direction of motion of erupting plasma.

3.2.2. Plasma Eruption

During the X2.2 flare, eruption of plasma was observed in different AIA channels. Interestingly, plasma eruption was more prominent in AIA filters sensitive to high temperatures. We have produced a series of AIA 94 Å running difference images for clear display of plasma ejection during this flare (Figures 4(a)–(d)). We readily observe plasma eruption toward the southwestern direction from the sigmoid (black arrows in

Figures 4(a)–(d) indicate the direction of erupting plasma). The amount and direction of plasma flow inferred from AIA images confirm its association with the CME detected by LASCO at 11:00 UT (top panels of Figure 2).

3.3. X9.3 Flare

3.3.1. Flare Evolution

After the first flare, the AR was quiet for about 2.5 hr, and then it produced the largest flare of this decade of class X9.3. Figure 5 displays different phases of the flare in AIA 94 Å images. In the preflare phase (Figures 5(a)–(c) and Figure 1(b)), we did not find any significant variation in morphology and intensity of emission within the sigmoid. With the flare onset (Figure 5(d)), we found that the filament, which had gone through the activation phase during the earlier flare of class X2.2, again intensified and appeared brighter than the rest of the sigmoid. The AIA 94 Å emission peaked at ∼12:05 UT (Figure 1(b)). Images taken during the impulsive and peak phases, following the eruption of the heated filament, reveal enormous increase of brightness in the flaring area (Figures 5(e)–(f)). After ∼12:05 UT, the flare entered in the gradual phase, where its intensity started to decrease both in *GOES* channels and AIA light curves (see Figure 1(b)). During this time, we identified an interesting feature occurring in the upper-right portion of the sigmoid (i.e., the elbow region; indicated by the boxes drawn with dashed lines in Figures 5(g)–(i)). The elbow exhibited a semicircular extension at the very northern end of the sigmoid from where plasma was observed to erupt during the declining phase of the flare. By 12:30 UT, intensity of the emission from the sigmoid decreased significantly, and we found a local minimum in the AIA 94 Å light curve at ∼12:30 UT (which can also be noticed in other AIA light curves). After this time, bright coronal loops in the northern part of the sigmoid started to expand, causing the intensity to increase in the AIA light curves again. The sigmoid with bright coronal loops in the northern part is shown in Figures 5(j)–(l). In Figure 5(l), from the HMI overplotted contours, one can easily infer that the postflare loop arcade connected the northern negative magnetic polarity region to the central positive magnetic polarity region.

Figure 6 contains a series of AIA 304 Å images displaying the different phases of the X9.3 flare. Before ∼11:53 UT (Figures 6(a)–(c)), the AR did not show much activity, and only a few relatively less significant, compact, and localized brightenings were observed. The filament lying in the middle portion of the sigmoid started to brighten up from ∼11:53 UT, which resulted in the onset of the impulsive phase of the X9.3 flare. The filament, after going through a brief phase of rapid expansion at around 11:55 UT, eventually erupted at ∼11:56 UT. The whole process of the filament activation and eruption is nicely and sequentially portrayed in the zoomed cutouts of Figures 6(d), (e), (f), and (h) (the filament is indicated by green arrows in these panels). It is noteworthy that the flare reached its peak intensity earlier in 304 Å than in 94 Å emission by ∼4 minutes (see Figure 1(b)). Following the eruption of the filament, we observed the formation of two flare ribbons in the core region of the sigmoid (Figure 6(i); indicated by the white arrows in the zoomed cutout). The separation between these two inner flare ribbons increased slowly but continuously (see Figures 6(i) and (l)), and after ∼12:14 UT, the loops connecting these two flares ribbons became so bright that they outshone the ribbons. Eruption of plasma from the elbow part of the sigmoid was also observed in the 304 Å channel, which is shown in the dotted boxes in Figures 6(j), (k), and (m) (also by the arrow in Figure 6(m)).

The late decay phase of the flare (after ∼12:32 UT) is characterized by very interesting evolution of highly extended flare ribbons that encompassed the whole AR (marked by the black arrows in Figures 6(n)–(o)). In Figure 6(o), we outline these ribbons by white dotted lines. Interestingly, the development of extended flare ribbons was spatially and temporarily correlated with the formation of hot coronal loop arcade, as observed in the AIA 94 Å channel (see Figures 5(j) and (k)). Furthermore, the flux enhancement associated with the evolution of extended flare ribbons and overlying loop arcade can be readily seen from the EUV time profiles between ∼12:30 UT and ∼13:25 UT. It is interesting to note the loop arcade in AIA 304 Å images as well, which essentially implies the filling of plasma in low-lying loops at chromospheric temperatures. Furthermore, we note that very intense and diffuse emission from the loop arcade was observed in the AIA 94 Å channel, whereas AIA 304 Å images present a much more structured loop morphology (indicated by blue arrows in Figure 6(p)).

3.3.2. Plasma Eruption

Spectacular eruption of plasma was observed in different phases during the X9.3 flare. Immediately after the eruption of the filament at ∼11:56 UT, we observed plasma eruption at two predominant directions: southern (shown in Figures 4(f)–(h) by yellow arrows) and northwestern (indicated by blue arrows in Figures 4(f)–(i)). This first phase of the eruption ceased to exist after ∼12:03 UT in AIA 94 Å difference images (see Figure 4(j)). However, a second stage of plasma eruption started to appear after ∼12:08 UT and continued until ∼12:55 UT, whereas the flare had already entered in the late decay phase (indicated by red arrows in Figures 4(m)–(p)). As evident from the running difference images, this eruption mostly proceeded toward the northwestern direction. Here, we recall reorganization occurring near the elbow region of the sigmoid following the filament eruption. Apart from these prominent phases of plasma eruption noted already, we cannot ignore continuous plasma eruption from the sigmoidal region during the flare that exhibited relatively faint signatures in the running difference images.

3.4. DEM Analysis

We have thoroughly examined spatial distribution and structures of multithermal plasma during different phases in the evolution of the sigmoid by adopting DEM analysis. For this purpose, we utilize simultaneous observations in six coronal AIA channels (94 Å, 131 Å, 171 Å, 193 Å, 211 Å, and 335 Å). DEM, in the unit of $\mathrm{cm}^{-5}\ \mathrm{K}^{-1}$, is given by

$$\mathrm{DEM}(T) = n^2 \frac{dh}{dT} \tag{1}$$

where $n(h(T))$ is the electron density at height h and temperature T (see Chapter 4 of Mariska 1992). Line intensity, in unit of erg $\mathrm{cm}^{-2}\ \mathrm{s}^{-1}\ \mathrm{sr}^{-1}$, which can be directly measured by

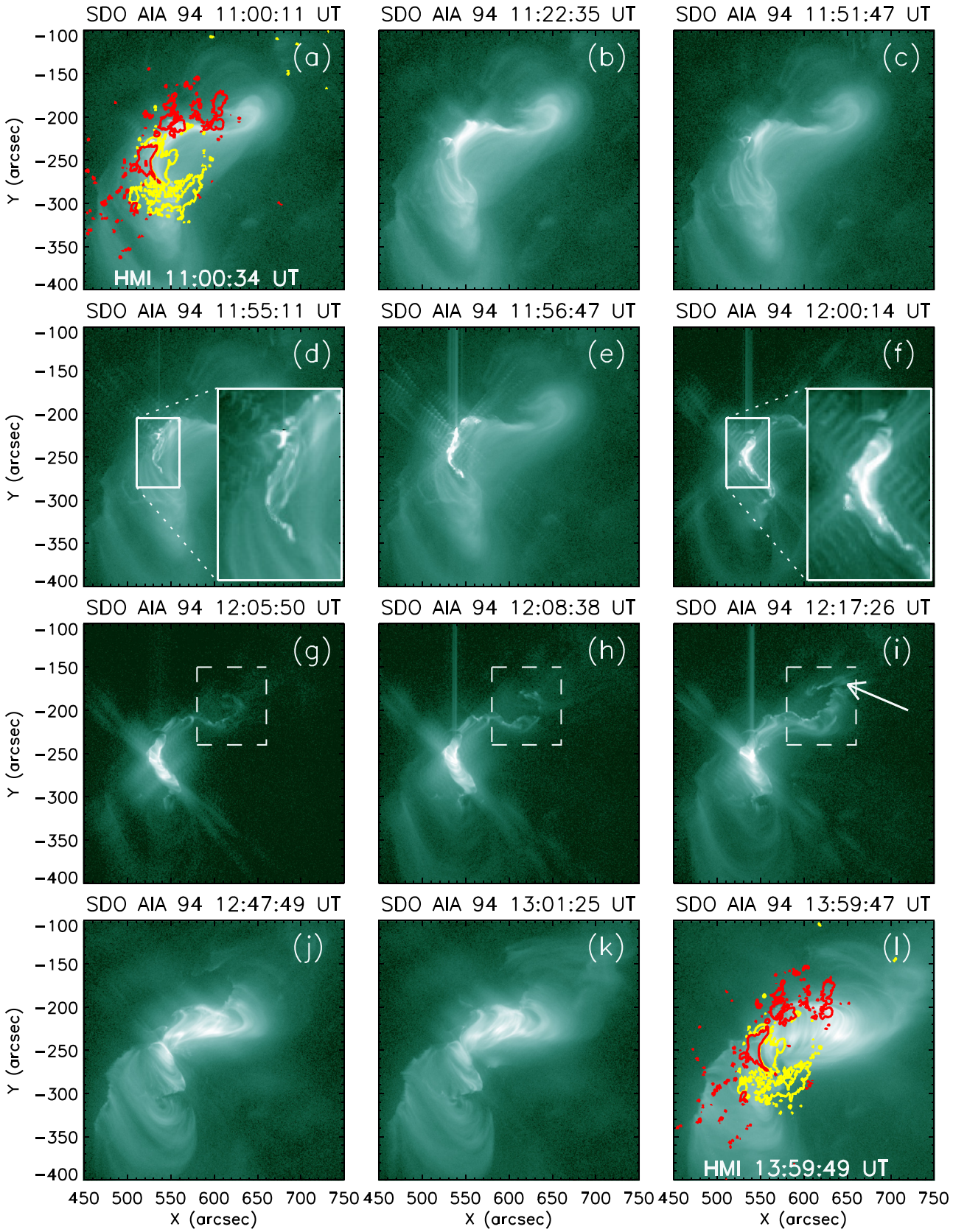

Figure 5. Sequence of AIA 94 Å images showing the evolution of the X9.3 flare. The inset in panel (d) shows a zoom of the central region of the sigmoid from where the flare was initiated. The inset in panel (f) shows a zoomed-in image of the brightest region during the peak emission of the X9.3 flare. Regions inside the dashed boxes in panels (g)–(i) show formation of a semicircular arc in the northern end of the AR. The arrow in panel (i) indicates eruption of plasma from the semicircular arc region. Contour levels of HMI LOS magnetogram in panels (a) and (l) are ±400 G, where yellow and red contours refer to positive and negative polarity, respectively.

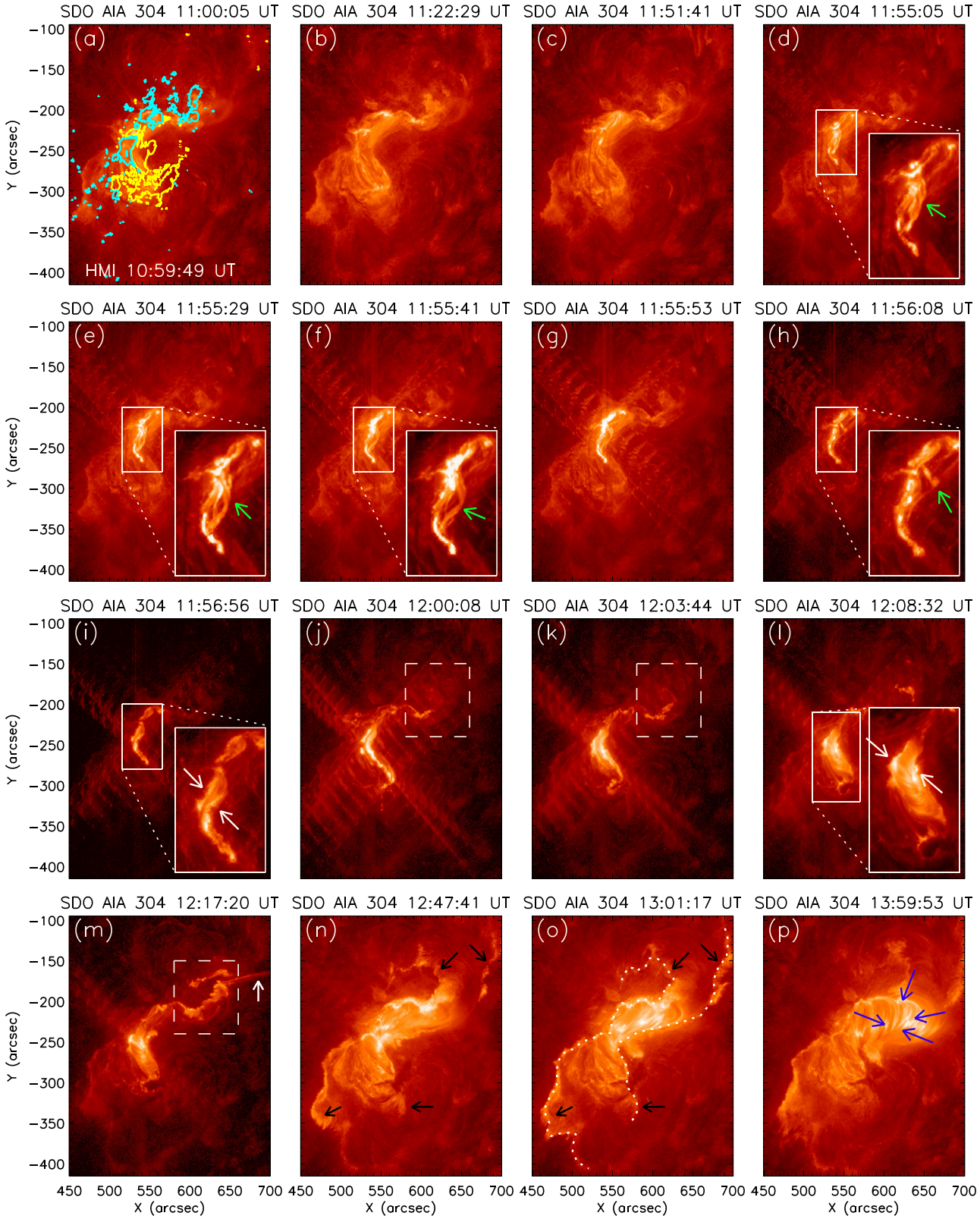

Figure 6. Sequence of AIA 304 Å images corresponding to the X9.3 flare. Insets in panels (d), (e), (f), and (h) sequentially show activation and eruption of the filament (indicated by green arrows). Insets in panel (i) and (l) show formation and separation of the two inner region postflare ribbons (indicated by the two white arrows in the insets). Regions inside the dashed boxes in panels (j), (k), and (m) show the semicircular arc formed during the gradual phase of the flare. The small arrow in panel (m) indicates erupting plasma from the semicircular arc region. Formation of extended postflare loops in the decay phase of the X9.3 flare is shown by black arrows in panel (n) and (o) and by the dashed curve lines in panel (o). Postflare arcades in the late decay phase are very clear in panel (p) (indicated by blue arrows). Contour levels of the HMI LOS magnetogram in panel (a) are ±400 G, where yellow and blue contours refer to positive and negative polarity, respectively.

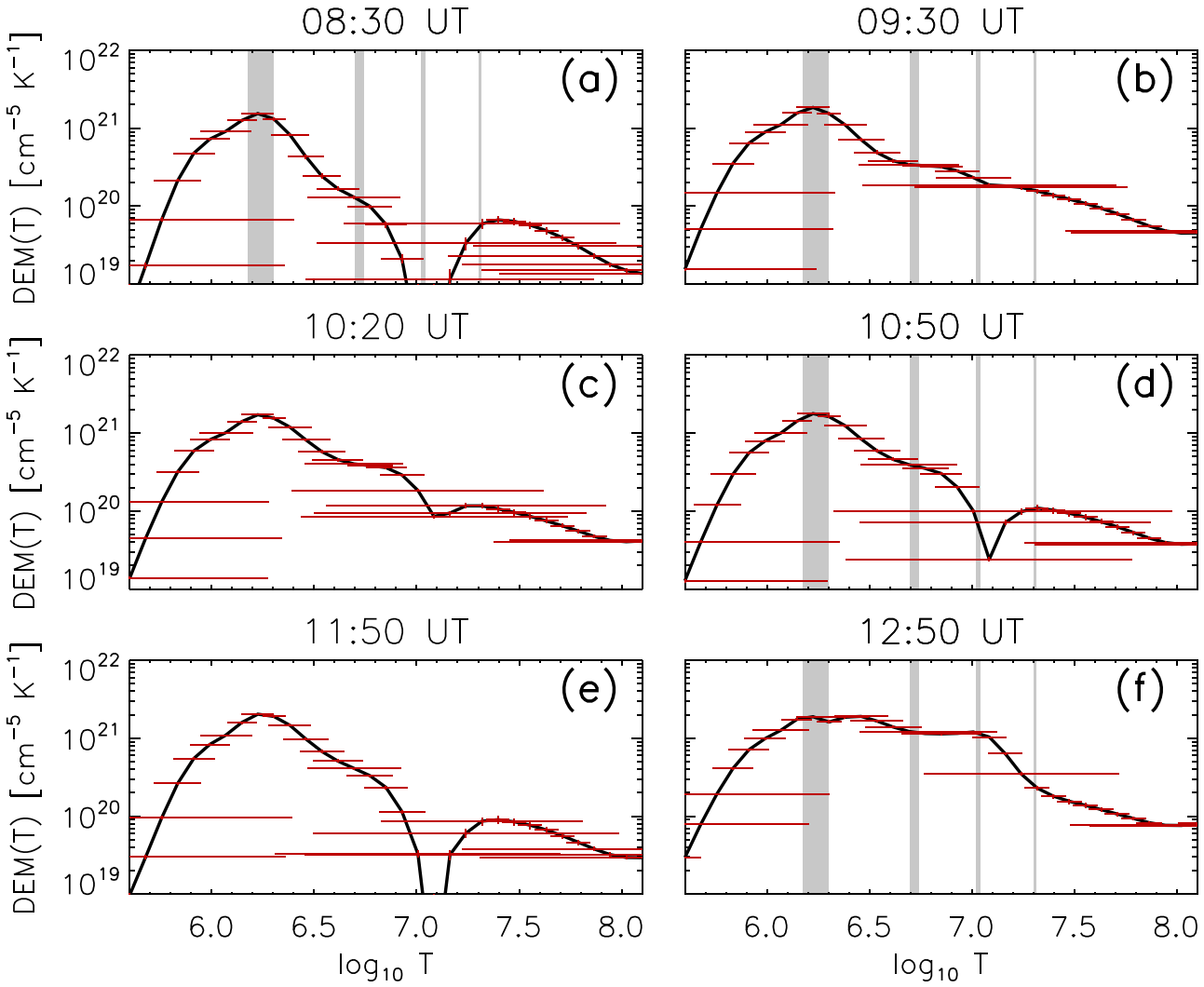

Figure 7. DEM profiles obtained from the overall AR at six selected times: before the X2.2 flare (panel (a)), after the impulsive phase of the X2.2 flare (panel (b)), between the two X-class flares (panel (c) and (d)), just before the initiation of the X9.3 flare (panel (e)), and after the impulsive phase of the X9.3 flare (panel (f)). The horizontal and vertical red line segments show uncertainty in temperature and DEM counts, respectively. Note that the vertical red lines showing uncertainty in DEM counts are very small compared to the horizontal lines because of the much larger range in DEM values (shown in the *Y*-axis) compared to the temperature values (shown in the *X*-axis). The gray strips in panels (a), (b), (d), and (f) indicate four selected temperature ranges, for which representative EM maps are given in Figure 8.

the telescope detectors, is given by

$$I_{ji} = h\nu_{ji} \int G(T)\ \mathrm{DEM}(T)\ dT + \delta I_{ji}, \tag{2}$$

where $G(T)$ is the temperature response function and j and i are atomic energy levels (i.e., the emission line is produced by the photons emitted due to the transition from j^{th} energy level to i^{th} energy level). δI_{ji} is uncertainty in measurement. Total emission measure in a given temperature range $[T_1, T_2]$ can be expressed as

$$\mathrm{EM} = \int_{T_1}^{T_2} \mathrm{DEM}(T)\ dT. \tag{3}$$

The AIA temperature response function can be found by using the SSW routine aia_get_response.pro. For DEM computation, we have used the regularization inversion technique developed by Hannah & Kontar (2012). The initial step to the process is to obtain perfect coalignment of AIA images in six coronal channels, which can be done by the SSW routine aia_coalign_test.pro. This routine produces outstandingly accurate results (the error being <1 pixel) by fitting limbs and makes the relevant changes in the header of the FITS file corresponding to the images (Aschwanden et al. 2013).

Figure 7 shows the DEM count from the AR as a function of temperature at different times. Before the X2.2 flare (Figure 7(a)), we found two peaks in the DEM curve: one around $\log(T) \approx 6.3$ and another one around $\log(T) \approx 7.4$. Between $\log(T) \approx 6.9$ and 7.2, DEM counts are very low. After the impulsive phase of the X2.2 flare (Figure 7(b)), DEM counts in this temperature range enhanced significantly and thereafter decreased continuously until the start of the X9.3 flare (Figures 7(b)–(e)). Following the impulsive phase of the X9.3 flare, DEM counts in this temperature range enhanced again (Figure 7(f)). In Figure (7), we also show uncertainties in temperature and DEM counts by horizontal and vertical red lines. We note uncertainty in temperature to be higher at low and very high temperature ranges (see temperature below log $(T) = 5.8$ and above $\log(T) = 7.8$ in Figure 7(a)). However, the uncertainties at high temperatures reduced significantly just after the impulsive phases of the two X-class flares because of

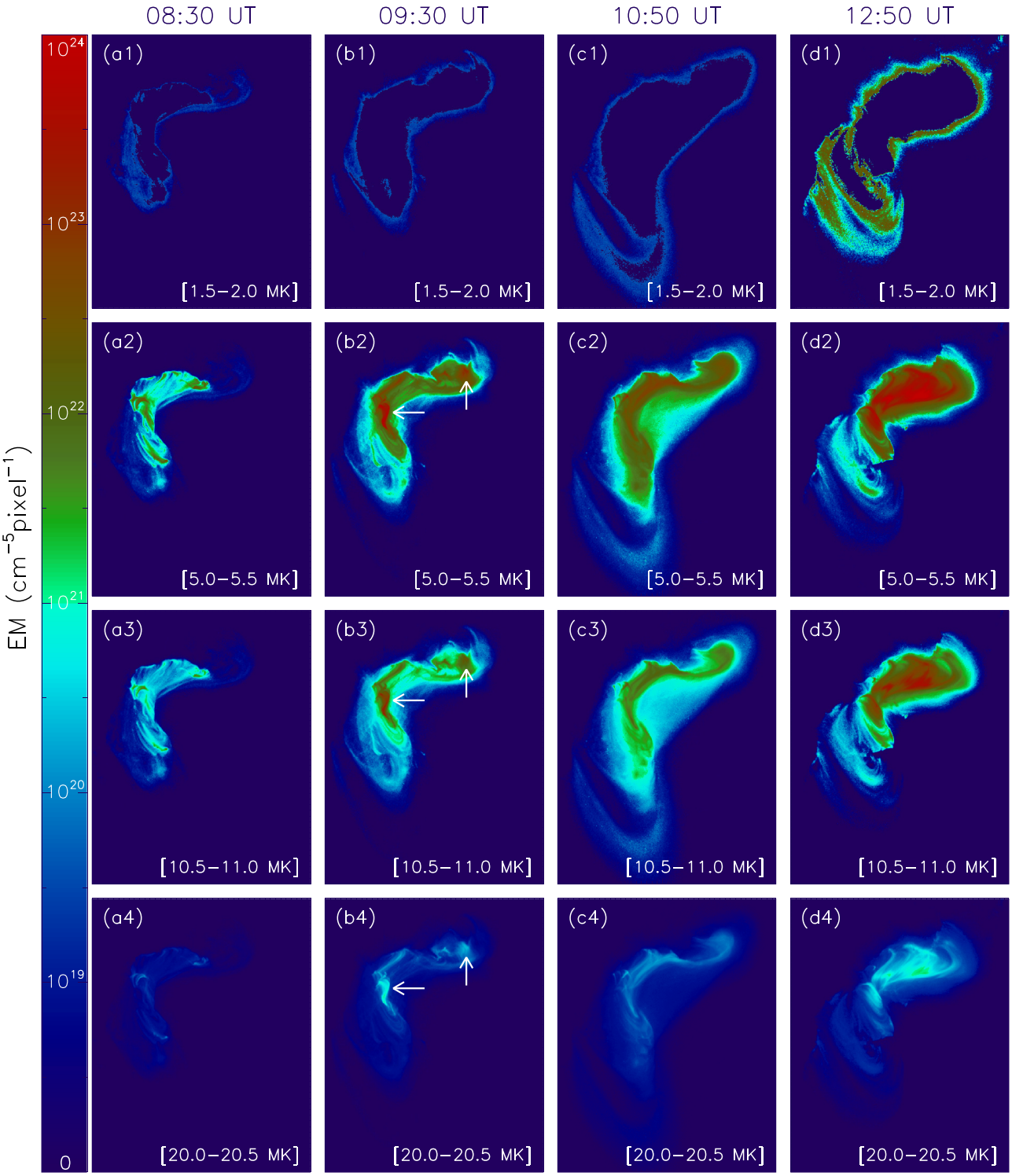

Figure 8. EM maps of the AR in different temperature ranges: 1.5–2.0 MK in row (a1)–(d1), 5.0–5.5 MK in row (a2)–(d2), 10.5–11.0 MK in row (a3)–(d3), 20.0–20.5 MK in row (a4)–(d4), before the X2.2 flare (column (a1)–(a4)), just after the X2.2 flare (column (b1)–(b4)), between the two flares (column (c1)–(c4)), and after the X9.3 flare (column (d1)–(d4)). The field of view of the EM maps is $(x_1, y_1) = (450'', -440'')$; $(x_2, y_2) = (700'', -150'')$. The four temperature ranges in these EM maps have been shown by shaded vertical strips in each of the panels (a), (b), (d), and (f) of Figure 7. In the panels of the first three rows, only those pixels with uncertainty both in DEM count and temperature less than 30% , are plotted. In the panels of the bottom row, pixels with uncertainties in DEM count less than 30% and temperature less than 50% are plotted.

large enhancement of the overall emission of hot flaring loops from the AR.

For further understanding of plasma emission from the flaring region, we have plotted EM maps at four selected times (Figure 8) in different temperature ranges (indicated by the vertical strips in Figures 7(a), (b), (d), and (f)). The first column of Figure 8 (panels (a1)–(a4)) represents emission maps corresponding to the quiet phase of the AR (i.e., before the

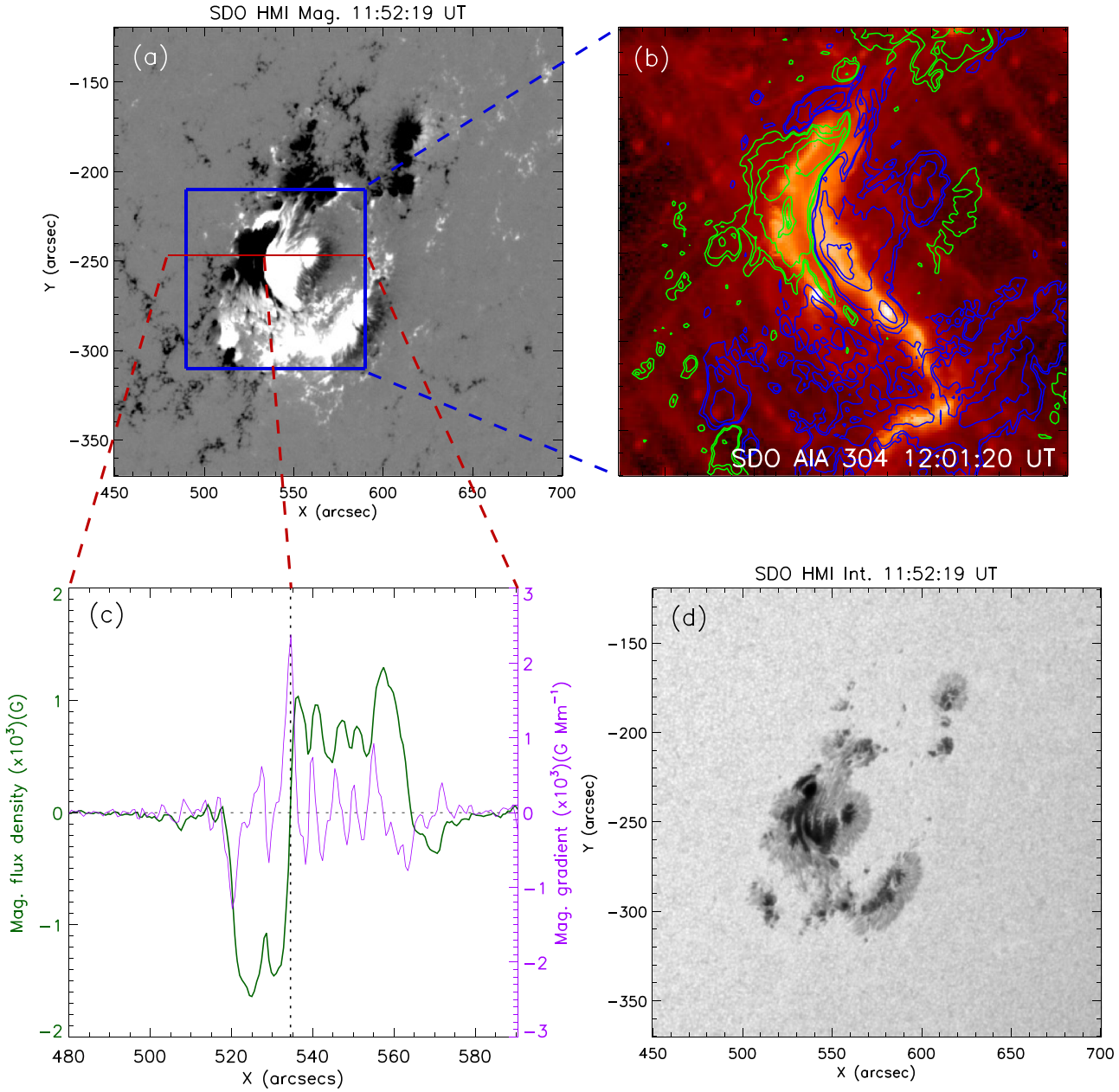

Figure 9. Panel (a): HMI LOS magnetogram of AR 12673. The X-class flares occurred in the central region of the AR, which is indicated by the blue box. Panel (b): AIA 304 Å image of region showing the extent of inner flare ribbons during the impulsive phase of the X9.3 flare with contours from the LOS magnetogram overplotted. Contour levels are ±(300, 500, 1000, 1500) G, with blue and green contours referring to positive and negative polarity, respectively. Panel (c): magnetic flux density (green) and magnetic gradient (purple) computed along the red slit in panel (a). Panel (d): white light image of the AR showing multiple, fragmented umbrae within conjugated penumbrae.

X2.2 flare). At a lower temperature range (1.5–2.0 MK; Figures 8(a1)–(d1)), emission is seen to be predominantly produced from the outer regions of the sigmoid. This is acceptable because emission from a quiet corona lies in this temperature range. We found that a moderate amount of hot plasma existed in the sigmoid region before the flaring activities (Figures 8(a2) and (a3)). During the X2.2 flare, we found enhancement of emission measure at the core and northern elbow region (Figures 8(b2)–(b4)). Before the onset of X9.3 flare, the sigmoid underwent significant spatial expansion (Figures 8(c2)–(c4)). During the X9.3 flare, we noted large enhancement in the emission measure of hot plasma at the northern part of the sigmoid, whereas the southern part was highly structured.

3.5. Magnetic Structure of AR 12673

In Figure 9(a), an HMI LOS image of the AR is plotted. In the northern part of the AR, we found that negative polarity magnetic regions predominantly existed, whereas positive polarity structures were fewer and very dispersed. In the southern part of the AR, positive polarity regions strongly dominated over negative polarity regions. In the middle portion of the AR, we found strong regions of negative and positive polarities in a conjugated state. This was the most eventful region, being associated with activation and eruption of the filament along with early flare ribbon brightenings during the X-class flares (see Figure 9(b); also seen in Figures 3, 5, and 6). The blue box in Figure 9(a) encloses the photospheric region, which was associated with inner ribbon brightening. In

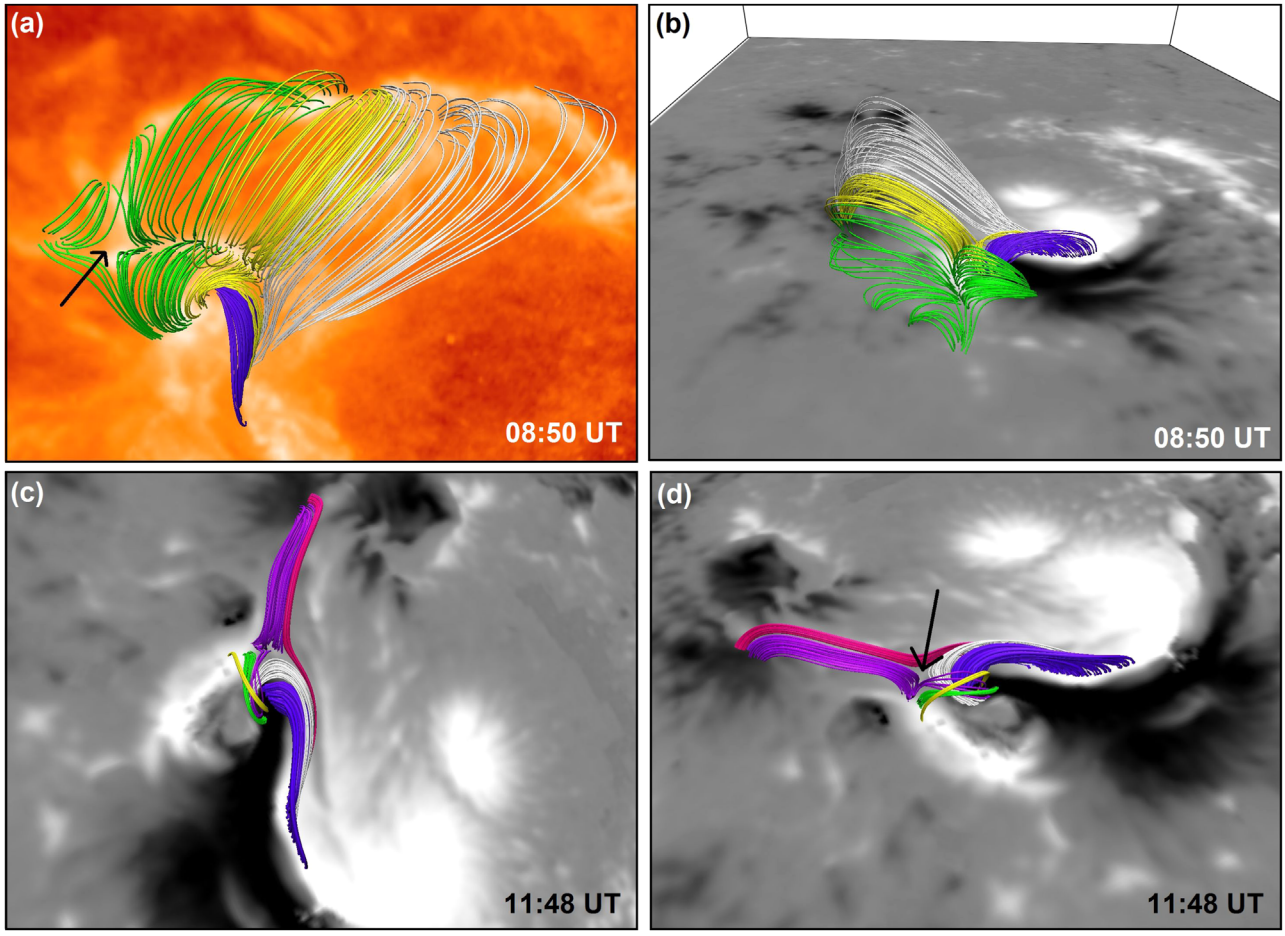

Figure 10. NFFF extrapolation showing model coronal magnetic field structures of the AR. In panels (a) and (b), we show top and side views, respectively, of the coronal magnetic fields before the X2.2 flare (08:50 UT) associated with the core region of the sigmoid (i.e., high magnetic gradient region) and remote preflare ribbon-like brightenings. In panels (c) and (d), we focus on the coronal magnetic configuration at the core region before the X9.3 flare (11:48 UT) with its top and side views, respectively. For clarity in representation, we have used different colors to show the model field lines. Background of panel (a) represents cotemporal AIA 304 Å image, whereas in panels (b)–(d), cotemporal HMI LOS magnetograms are plotted as background. We found a twisted set of field lines lying over the PIL, in the region of high magnetic field gradient (indicated by blue lines in panels (a)–(d)), that resembles a magnetic flux rope. Black arrows in panels (a) and (d) indicate X-type null.

Figure 9(b), we present an overplot of AIA 304 Å image with HMI LOS magnetogram to show the extension of flare ribbons with respect to the photospheric magnetic configuration during X9.3 flare. To estimate the magnetic field gradient across the PIL, we have considered a slit across the AR (the red line in Figure 9(a)) along which magnetic field strength and magnetic gradient were calculated, which are plotted in Figure 9(c). We found a very sharp gradient in the magnetic field, with magnetic strength changing from about ∼–1000 G to ∼+1000 G over a distance of ∼1 arcsec (the peak gradient being $\sim 2.4 \times 10^3$ G Mm^{-1} on the PIL). In Figure 9(d), a continuum image of the AR is plotted, in which multiple, segmented umbrae can be found in the central region of the AR surrounded by a single penumbra. Comparison of the magnetogram and continuum images of the AR confirms that, before the X-class flares, AR 12673 had evolved into a complex δ-spot configuration.

4. Magnetic Field Modeling

To understand the magnetic field topology of the AR, we extrapolated magnetic field lines using the NFFF technique (Bhattacharyya et al. 2007; Hu & Dasgupta 2008; Hu et al. 2008). For completeness, we provide a brief discussion of the technique in the Appendix.

4.1. Preflare Configurations

The modeled magnetic field configuration before the X2.2 flare (Figures 10(a) and (b)) reveals the preexistence of a flux rope at the core of the sigmoid that extends over the PIL with a north–south orientation (shown in blue lines in Figures 10(a) and (b)) with northern and southern footpoints fixed at negative and positive polarity regions, respectively. Comparison of magnetic field extrapolations with preflare brightenings observed in AIA 304 Å image (Figure 10(a)) reveals a very consistent picture, in which ribbon-like extended preflare brightenings seen in the north of the core region are formed at the footpoints of model AR loops that terminate at the core region (shown in green, yellow, and white lines in Figures 10(a) and (b)). Furthermore, extrapolated field lines near the northern footpoints of the flux rope reveal a magnetic null (indicated by the black arrow in Figure 10(a)), which is regarded as a potential site for magnetic reconnection.

The overall preflare magnetic configuration, derived from the extrapolation, for the X9.3 flare at the core region of the

sigmoid (Figures 10(c) and (d)) remains similar to that of the earlier X-class flare. Notably, the extrapolation shows the presence of a magnetic null (shown by the black arrow in Figure 10(d)) along with an X-type configuration (yellow and green lines in Figures 10(c) and (d)) at this time. Furthermore, we found that field lines involved in the X-type configuration seemed to provide tethering to the flux rope near its northern footpoint.

4.2. Magnetic Configurations of the Inner and Extended Flare Ribbons during the X9.3 Flare

As noted in Section 3.3.1, the X9.3 flare was characterized by a pair of inner ribbons during the impulsive phase, whereas extended ribbons appeared in the late phases (Figures 11(a) and (b)). In Figure 11, we show model coronal field configuration at the location and timing of the inner (12:08 UT) and extended (12:50 UT) flare ribbon structures. Extrapolations suggest the formation of a low-lying system of a highly sheared set of postflare loops in the inner ribbon area (Figure 11(d)) that was occupied with the model flux rope during the preflare phase of the X9.3 flare (Figures 10(c) and (d)). Comparison between the extended ribbon structures during the late phase (12:50 UT) and extrapolated coronal field lines establish connectivities between opposite polarity ribbons by large overlying loop systems (Figure 11(e)). Connectivity in the northern part of the extended postflare ribbons (shown in the box (I) in Figure 11(b)) is shown by the green model field lines in Figure 11(e), whereas the southern part of the extended ribbons (shown in the box (II) in Figure 11(b)) is connected by the yellow model field lines (Figure 11(e)). Pink model lines in Figure 11(e) establish connectivities within the core region of the sigmoid in the late phase. Interestingly, the model postflare coronal loops at the central region of the sigmoid (blue lines) nicely resemble the dense loop arcade observed in the AIA 304 Å images (see Figures 11(c) and (e)).

4.3. Free Magnetic Energy in the AR

The magnetic free energy (E_F) associated with an AR can be estimated by the difference of nonpotential magnetic energy (in this case, NFFF magnetic energy (E_{NFFF})) and potential magnetic energy (E_P) (i.e., $E_F = E_{NFFF} - E_P$). In Figure 12, we show variation of the normalized magnetic free energy (E_F/E_P) for the extrapolated field from 08:30 UT to 14:00 UT, which includes the two X-class flares. The shaded regions indicate the main energy release phases of the two X-class flares, as identified in the *GOES* SXR band of 1–8 Å (shown by the blue curve in Figure 12). Clearly, the free energy of the AR decreased after both the X-class flares. As expected, the decrease in free energy observed was larger after the X9.3 flare than the earlier X2.2 flare.

We note that the free energy available in the AR before the eruptions was ∼82% and ∼80% of the potential energy for X2.2 and X9.3 flares, respectively. These estimates seem to be higher than those for typical ARs producing X-class flares. Several assessments concerning X-class events reveal the free energy to be ∼30%–50% of the potential energy (Jing et al. 2010; Sun et al. 2012; Choudhary et al. 2013; Muhamad et al. 2018). Although the availability of free magnetic energy is unambiguously a prerequisite for flare occurrence, it alone may not ensure the flare onset (see e.g., Jing et al. 2010). We also emphasize that NOAA AR 12673 was an extraordinary AR that produced four X-class and 20 M-class flares within 6 days, while exhibiting a δ-type magnetic configuration. Furthermore, on 2017 September 6, two X-class flares (studied here) occurred very close in time (within ∼3 hr), with the latter being the largest flare of the solar cycle, thus signifying the large excess of free magnetic energy of the AR 12673.

5. Discussion

In this article, we present a multiwavelength investigation of two X-class flares from the AR NOAA 12673 that occurred within an interval of about 3 hr (see Figure 1). Notably, the second flare of X9.3 class turned out to be the largest flare in solar cycle 24. Both flares were eruptive in nature (Figures 2 and 4).

The AR NOAA 12673 was highly flare productive.[5] It appeared in the eastern limb of the Sun on August 28 as a simple α-type AR and gradually evolved into complex $\beta\gamma$-type on September 4. It became an even more complex $\beta\gamma\delta$-type on September 5 and remained so until its disappearance over the western limb of the Sun on September 10. In total, it produced 27 M-class and 4 X-class flares between September 4–10. Following the occurrence of the two X-class flares on September 6, reported in this article, it went on to produce an X1.3-class flare on September 7 and an X8.2-class flare on September 10 besides several M-class major eruptive events. During the occurrence of X-class flares, the complex AR had shown δ-sunspots, which are identified with a complex distribution of sunspot groups in which the umbrae of positive and negative polarities share a common penumbra (Künzel 1960). Such complex ARs are known to produce powerful flares (see e.g., Zirin & Liggett 1987; Sammis et al. 2000; Takizawa & Kitai 2015). It is noteworthy that AR 12673 was a rather compact region (Figure 9) that displayed more spatial extension in the north–south direction than the usual east–west direction. The δ-sunspots were concentrated at the central part of the AR where magnetic fields were very strong, and the magnetic field gradient across the PIL was extremely high ($\sim 2.4 \times 10^3$ G Mm^{-1}; see Figure 9(c)). Earlier studies have shown a close relationship between major flare activities and strong magnetic field, especially those with a high gradient and those that are highly sheared across the PIL (Hagyard et al. 1984; Zirin & Wang 1993; Schrijver 2007; Barnes et al. 2016). The reported eruptive activities in AR 12673, thus, represent the capability of the AR in the rapid generation and storage of huge amount of excess magnetic energy in the corona. In this context, the evolution of normalized free magnetic energy during the X-class flares is noteworthy (Figure 12). We found that the free magnetic energy stored in the AR before the flaring activity was ∼82% of the potential magnetic energy. After the two X-class flares, it reduced to ∼70%. Our analysis, therefore, implies that a large amount of free magnetic energy was already stored in the AR before the flaring activities and that the large X-class flares essentially released only a small fraction of it.

The observations of the AR in the AIA 94 Å channel (6 MK) clearly show the preexistence of a coronal sigmoid, which is considered to be an indicator of twisted or helical magnetic structures (Gibson et al. 2002). Coronal sigmoids, originally discovered in soft X-ray emission (Manoharan et al. 1996; Rust & Kumar 1996), were eventually identified as potential sites for

[5] https://www.swpc.noaa.gov/products/solar-region-summary

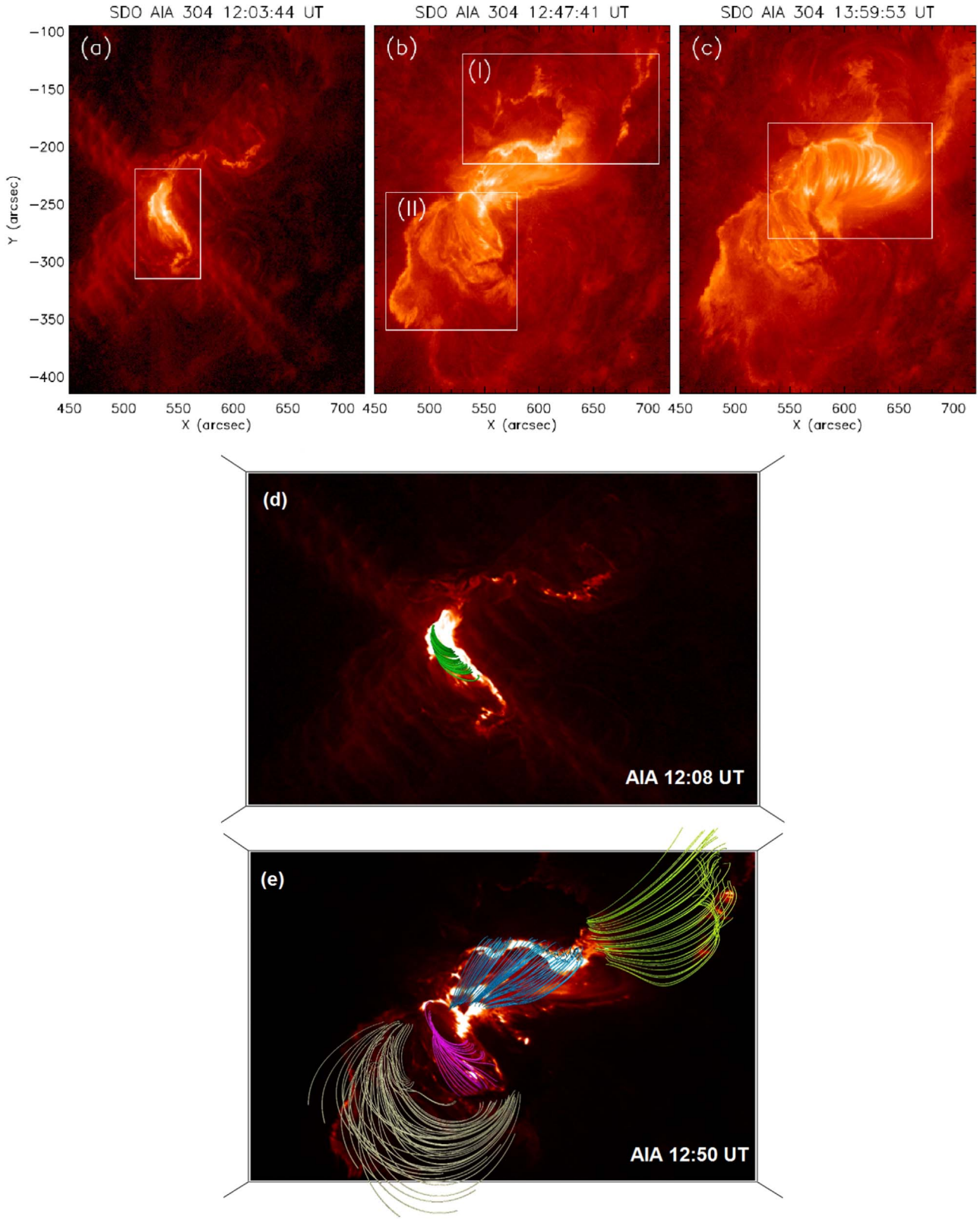

Figure 11. Panels (a)–(c): AIA 304 Å images showing the inner flare ribbons, extended flare ribbons, and postflare loop arcades, respectively. Panel (d): model coronal magnetic field configuration showing connectivity between the inner flare ribbons (also indicated by the box in panel (a)). Panel (e): model coronal field configuration showing connectivities among different parts of extended ribbon structures by green and yellow lines (see, regions marked by box (I) and (II)) in panel (b) and in the region of dense postflare arcade by blue lines (also indicated by the box in panel (c)). Pink model lines in panel (e) show connectivity in the core of the AR in the late decay phase of the X9.3 flare.

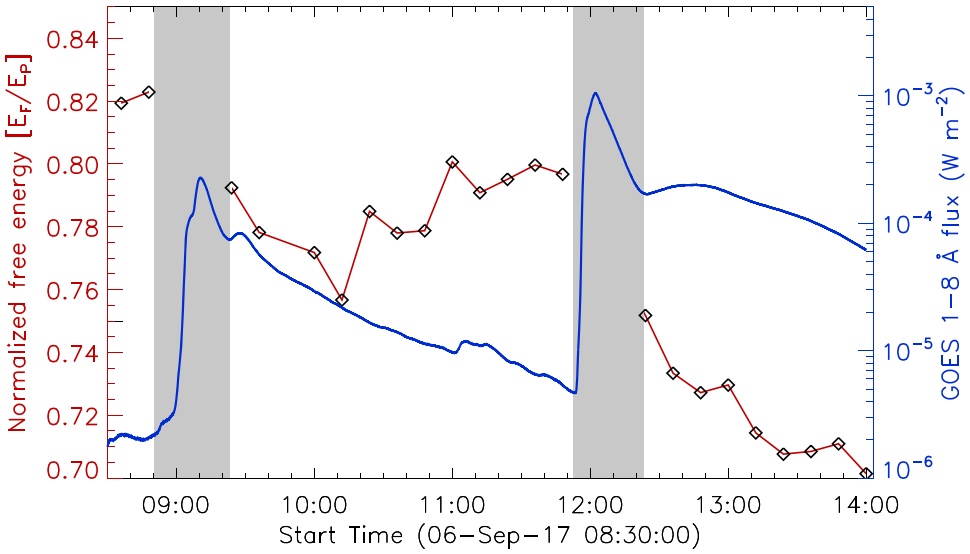

Figure 12. Time variation of normalized free magnetic energy in the AR NOAA 12673 (shown by the red curve) on 2017 September 6 from 08:30 UT to 14:00 UT. Normalized free energy is computed by taking the difference between NFFF magnetic energy and potential magnetic energy, normalized by the corresponding potential magnetic energy (i.e., $\frac{E_F}{E_P}$). For a comparison, *GOES* 1–8 Å flux profile in the same duration is shown by the blue curve, which indicates the occurrence of two X-class flares. The shaded regions indicate the main energy release phase of the two X-class flares during which the intense flare emission caused artifacts in the measurement of the photospheric magnetic field, making the calculations of magnetic energy unreliable.

CMEs (Canfield et al. 1999). Later on, sigmoid type ARs were confirmed in numerous EUV observations (Sterling et al. 2000; Liu et al. 2007, 2010; Joshi et al. 2017, 2018; Green et al. 2018). Following the eruption of the flux rope, sigmoid structures are observed to undergo major reorganization and the region is enveloped by a set of bright postflare loop arcades or cusped loops. Thus, the sigmoid-to-arcade development is suggestive of large-scale magnetic reconnection driven by the eruption of the sheared core fields (Sterling et al. 2000). Our observations reveal a sigmoid structure before the first X-class flare that remained intact after the event (Figure 3). However, the sigmoidal region completely transformed into the postflare arcade in a sequential manner during the second X-class flare (Figures 5 and 6). The present observations thus indicate the occurrence of two eruptive X-class flares within a single sigmoid-to-arcade event, which does not seem to be a commonly observed phenomenon. In a comprehensive study of a major geomagnetic effect caused by two ultra-fast CMEs in 2012 March, Patsourakos et al. (2016) found that the two CMEs were linked with two X-class flares occurring from the same AR (NOAA 11429) within an interval of ∼1 hr. However, unlike our studied events, the two X-class flares were initiated from different locations of the AR and were associated with two separate sets of postflare arcades.

Soon after the eruption of the flux rope from the central portion of the AR during the impulsive phase of the X9.3 flare, the formation of two flare ribbons on the either side of the PIL was observed in AIA 304 Å images (the inner flare ribbons; see Figure 6(i)). We note that the flare ribbons developed during the previous X2.2 event also appeared at the same part of the AR (i.e., on either side of the high magnetic gradient region along the PIL) (Figure 3(j)). It is noteworthy that these inner flare ribbons were subjected to very little separation, which is rather uncommon in strong eruptive X-class flares. We attribute this small separation between flare ribbons to the fact that footpoints of the flare loops were rooted in δ-sunspot regions of strong magnetic field $\boldsymbol{B}$. Thus, although the loop growth and inner ribbon expansion speed $\boldsymbol{v}$ were small, the associated local reconnection rate (coronal electric field, i.e., the rate at which field is brought into the reconnection region), which can be derived from the observations of the flare ribbons as $\boldsymbol{E}_c = \boldsymbol{v} \times \boldsymbol{B}$ (Forbes & Priest 1984), would have been large enough to produce X-class events. This is supported by the finding of the recent statistical analysis of reconnection rates in solar flares over four orders of flare magnitude (from B to X17) by Hinterreiter et al. (2018), who showed that the correlation of the local reconnection rate with flare class is a stronger function of the underlying field strength $\boldsymbol{B}$ than the flare ribbon separation velocity $\boldsymbol{v}$ (see Figure 10 therein).

We performed DEM analysis to probe various temperature structures of the sigmoid (Figure 8). Our analysis revealed that the temperature distribution of the sigmoid was very structured. Interestingly, the core of the sigmoid was observed to produce high-temperature emission, even before the flare activities, whereas the outer regions of the sigmoid were seen at lower temperatures. The preflare heating of the sigmoid is likely due to the localized events of small-scale, slow reconnections that may occur in response to the flux cancellation at the PIL (Moore & Roumeliotis 1992). The core of the sigmoid expanded during the X-class flares, which is attributed to strong heating by large-scale magnetic reconnections. We further note that the sigmoid region was already very heated before the X9.3 flare. This preheating of plasma could significantly contribute toward enhancing the efficiency of the particle acceleration process associated with subsequent flare emission. EM maps also reveal the substantial volume of hot (>10 MK) plasma during the postflare phase of the X9.3 event.

NFFF modeling of coronal magnetic field lines clearly shows a twisted set of magnetic field lines at the core of the sigmoid, which can be clearly identified as a flux rope (Cheng et al. 2014). We note intense short loops that seem to tether the middle region of the sigmoid (Figure 3(b)). Notably, this region intensified highly during the impulsive phase of the flares (Figures 3(c)–(f) and Figures 5(e)–(g)). We identify this as the core of the sigmoid that lay over the region of very high

magnetic gradient and high nonpotentiality. The tether of the flux rope is apparently enveloped by the short, low-lying magnetic loops (Figure 10), which suggests a close match between observed and modeled coronal loops. Our magnetic extrapolation analysis also successfully reveals magnetic connectivity between highly sheared core fields, close to the flux rope, and preflare ribbon-like brightenings observed in the 304 Å channel (Figure 10(a)).

We emphasize that both the X-class events not only occurred at the same region but also shared a common initiation process. The trigger happened at the central part of the sigmoid (Figures 3(c)–(e) and Figures 5(e)–(g)) that spatially lay close to the northern edge of the high magnetic gradient area (Figure 9) and was subjected to intense heating subsequently (Figure 8). The detection of preexisting magnetic null, close to the northern edge of the flux rope structure, in the extrapolated field lines (Figure 10) has important implications in understanding the triggering mechanism for the subsequent eruptive events. The synthesis of observed and modeled coronal loops/field lines provides concrete evidence that the location of the initial energy release is spatially correlated with the site of the magnetic null. In several contemporary studies on solar eruptions, it is widely accepted that a three-dimensional magnetic null provides a favorable configuration for magnetic reconnections. We thus believe that the triggering mechanisms for the eruptive events under this study are consistent with the breakout model (Antiochos et al. 1999) of solar eruptions. The observations of preflare ribbon structures that were magnetically connected to the core region (Figure 10(a)) further strengthen the case for the breakout scenario, because the overlying field lines would channelize the flow of particles, accelerated in the breakout current sheet, to remote footpoints. However, unlike in the case of the classical breakout model, here preflare reconnection seems to have occurred at relatively lower coronal heights. Our observations indicate that the triggering reconnections at the magnetic null were capable of destabilizing the flux rope only locally during the first X-class flare because the eruption was relatively minor and the overall sigmoid structure was preserved. This could happen because of the strong field lines lying over the flux rope, as well as firm tying of its southern footpoint. The coronal conditions seem to become conductive for the complete eruption by the time of the second X-class flare, which resulted in the eruptive phenomena at much larger scales. Notably, the X9.3 flare exhibited two well-separated sets of large flare ribbons, the inner and outer ones, during the impulsive and declining phases, respectively, which implies that the reconnection in the overlying loops during the respective stages progressed at different heights in the corona. The brightening within the inner flare ribbon area marked the peak phase of this large X9.3 flare. On the other hand, the growth of the outer flare ribbons was accompanied by a complete restructuring of the sigmoidal region with the successive formation of a postflare arcade. Thus, the evolution of the inner and the outer flare ribbons signify the role of large-scale magnetic reconnection in this long-duration event.

As the flares progressed, the AIA 94 Å images revealed outward-moving arc-like high-temperature plasma structures that are termed hot channels in the contemporary literature (Cheng et al. 2013; Patsourakos et al. 2013; Nindos et al. 2015; Cheng & Ding 2016; Joshi et al. 2017). The AIA 94 Å running difference images unambiguously detect a hot channel eruption during both X-class flares (Figure 4), which is particularly prominent for the second event. The EUV hot channels have been accepted as evidence of magnetic flux ropes and, therefore, perhaps the earliest signatures of a CME in low corona (see e.g., Cheng et al. 2013; Patsourakos et al. 2013; Joshi et al. 2017), which is also supported by our observations.

In summary, our detailed study of two X-class flares from AR 12673, within a single sigmoid-to-arcade event, has provided important insights into the processes that are associated with the triggering of flux rope eruption and subsequent energy release processes. We found the inner region of the sigmoid to be at much higher temperatures compared to its outer regions, and it also showed structured plasma emission even during the preflare phase. During the first X-class flare, the core region of the sigmoid attained very high plasma temperatures that persisted afterward, whereas during the second flare, the intense brightenings at the core further extended outward, suggesting acceleration of the electrons and subsequent energy deposition by them occurring at much higher scales during the second event. The eruption of the hot EUV plasma channel during the flares and their subsequent expansion and outward propagation provide evidence of flux rope eruptions as the earliest signatures of CME from the source region. The preexistence of the flux ropes at the high magnetic field gradient region at the core of the sigmoid, identified in the NFFF modeling of the coronal magnetic field, is well supported by the subsequently observed eruptive expansion of hot EUV plasma channels that also originated from the core region. Our observations support the breakout model of solar eruptions. The second X-class flare diverged from the standard flare model in the evolution of two sets of flare ribbons that are spatially well separated, inner and outer ones, providing firm evidence of magnetic reconnections at two coronal heights involving low-lying and higher coronal loop systems, respectively. We conclude that the very high magnetic gradient across the PIL and excessive storage of nonpotential energy in the AR were the main cause behind the repeated strong flaring activity in the δ-sunspot configuration of AR 12673.

We thank the *SDO* team for their open data policy. *SDO* is NASA's mission under the Living With a Star (LWS) program. We are also thankful to Q. Hu for sharing the NFFF extrapolation code with us. This work is supported by the Indo-Austrian joint research project No. INT/AUSTRIA/BMWF/ P-05/2017 and OeAD project No. IN 03/2017. A. M.V also thanks the Austrian Science Fund (FWF): P27292-N20. We acknowledge the constructive comments and suggestions of the anonymous referee, which improved the scientific content and the presentation of the article.

Appendix
The Non-force-free-field Extrapolation

The advocacy of the NFFF extrapolation finds its root in the following dimensional analysis:

$$\frac{|\boldsymbol{j}\times\boldsymbol{B}|}{\left|\rho\frac{dv}{dt}\right|}\sim\frac{B^2}{L}\frac{t}{\rho v}\sim\frac{B^2}{\rho v^2}\sim\frac{B^2}{\rho {v_{\rm th}}^2}\frac{v_{\rm th}^2}{v^2}\sim\frac{1}{\beta}\frac{v_{\rm th}^2}{v^2} \quad (4)$$

where $v_{\rm th}$ and $\boldsymbol{j}=\nabla\times\boldsymbol{B}$ are the thermal velocity and the volume current density, respectively. The speed of the photospheric flow is generally accepted to be $\sim$1 km s^{-1} (Vekstein 2016; Khlystova & Toriumi 2017), and a straightforward

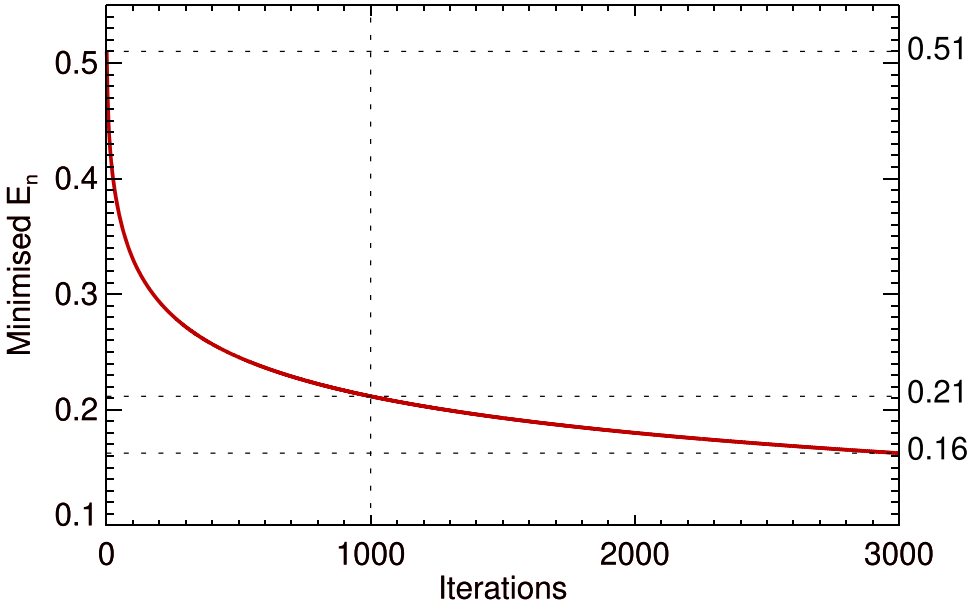

Figure 13. Variation of minimized deviation (E_n) with number of iterations corresponding to NFFF extrapolation for the case of the AR NOAA 12673 on 2017 September 6. E_n decreases monotonically to reach a value of 0.2 asymptotically for 1000 iterations. To save the computational cost, we have used the NFFF code for magnetic extrapolation up to 1000 iterations in this article.

calculation finds the thermal speed of the photospheric plasma to be also $\sim$1 km s^{-1}. Therefore, with $v_{\rm th} \sim v$ on the photosphere,

$$\frac{|\boldsymbol{j} \times \boldsymbol{B}|}{\left| \rho \frac{dv}{dt} \right|} \sim \frac{1}{\beta} \ . \tag{5}$$

In Equation (5), β is the ratio of thermal to magnetic pressure, which can be of the order of unity on the photosphere under an equipartition of kinetic and magnetic energies. Equation (5) then yields

$$|\boldsymbol{j} \times \boldsymbol{B}| \approx \left| \rho \frac{dv}{dt} \right|, \tag{6}$$

indicating the importance of the Lorentz force in conditions where $\beta \approx 1$.

The employed NFFF extrapolation uses an inhomogeneous double-curl Beltrami equation for the magnetic field $\boldsymbol{B}$,

$$\nabla \times \nabla \times \boldsymbol{B} + a \nabla \times \boldsymbol{B} + b\boldsymbol{B} = \nabla \psi \tag{7}$$

where a and b are constants. The scalar function ψ must be a solution of Laplace equation to make $\boldsymbol{B}$ solenoidal. A modified vector $\boldsymbol{B}' = \boldsymbol{B} - \nabla\psi$ (Hu et al. 2008) satisfies the corresponding homogeneous equation which, is known to represent a two-fluid MHD steady-state (Mahajan & Yoshida 1998) having a solution

$$\boldsymbol{B}' = \sum_{i=1,2} \boldsymbol{B}_i \tag{8}$$

where each $\boldsymbol{B}$ is a linear-force-free-field satisfying

$$\nabla \times \boldsymbol{B}_i = \alpha_i \boldsymbol{B}_i \tag{9}$$

in usual notations. The two sets of constants are related by $a = -(\alpha_1 + \alpha_2)$ and $b = \alpha_1\alpha_2$. The magnetic field is

$$\boldsymbol{B} = \sum_{i=1,2} \boldsymbol{B}_i + \boldsymbol{B}_3 \tag{10}$$

where $\boldsymbol{B}_3 = \nabla\psi$ is a potential field. Combining Equations (9) and (10),

$$\begin{pmatrix} \boldsymbol{B}_1 \\ \boldsymbol{B}_2 \\ \boldsymbol{B}_3 \end{pmatrix} = \mathcal{V}^{-1} \begin{pmatrix} \boldsymbol{B} \\ \nabla \times \boldsymbol{B} \\ \nabla \times \nabla \times \boldsymbol{B} \end{pmatrix} \tag{11}$$

where the matrix $\mathcal{V}$ is a Vandermonde matrix having elements α_j^{i-1} for $i, j = 1, 2, 3$ (Hu & Dasgupta 2008).

The procedure of NFFF extrapolation, described above, requires at least two layers of vector magnetogram since it involves the solution of a second order derivative, $\nabla \times \nabla \times \boldsymbol{B} = -\nabla^2\boldsymbol{B}$, at $z = 0$. This imposes a severe limitation in view of the availability of only one single-layer vector magnetogram. Thus, the NFFF solution is not unique and other solutions could exist on the same boundary condition. Therefore, the results of magnetic field modeling based on NFFF extrapolation should be viewed under this limitation. In view of this situation, we follow the technique proposed and demonstrated in Hu et al. (2008, 2010). In brief, starting with a selected pair of α and $B_3 = 0$, an optimal pair of α's is obtained by minimizing the average normalized deviation of the magnetogram transverse field ($\boldsymbol{B}_t$) from its extrapolated value ($\boldsymbol{b}_t$), namely

$$E_n = \sum_{i=1}^{M} |\boldsymbol{B}_{t,i} - \boldsymbol{b}_{t,i}| / \sum_{i=1}^{M} |\boldsymbol{B}_{t,i}| \tag{12}$$

where $M = N^2$ is the total number of grid points on the transverse plane. A fine tuning of E_n is further ensured by using $\boldsymbol{B}_3 = \nabla\psi$ as a corrector component field for the given pair of α's. Noting a superposition of potential fields being always potential, the above procedure is repeated until a minimal value of E_n is asymptotically achieved. For the extrapolations reported here, Figure 13 shows the variation of E_n with the number of iterations and documents its asymptotic approach to a minimal value. Auxiliary calculation (not shown) finds the

average intensity of the extrapolated photospheric magnetic field, related and prior to the X9.3 flare, is ≈1.2 kG. The corresponding $\beta \approx 0.97$ (for $n \approx 10^{23} m^{-3}$ (see, Priest 2014) and $T \approx 4000$ K, standard notations) substantiates the importance of the Lorentz force and makes the obtained extrapolated field, albeit nonunique, reliable.

Noteworthy is also the field line twist for the superposed $\boldsymbol{B}$. Twist can be quantified by the field-aligned current which, in this case, is given by

$$\tau \equiv \frac{\boldsymbol{j} \cdot \boldsymbol{B}}{|\boldsymbol{B}|^2} = \frac{(\alpha_1 \boldsymbol{B}_1 + \alpha_2 \boldsymbol{B}_2) \cdot (\boldsymbol{B}_1 + \boldsymbol{B}_2 + \boldsymbol{B}_3)}{(\boldsymbol{B}_1 + \boldsymbol{B}_2 + \boldsymbol{B}_3) \cdot (\boldsymbol{B}_1 + \boldsymbol{B}_2 + \boldsymbol{B}_3)} \ . \quad (13)$$

In addition to any modifications of α_1 and α_2, the twist τ can vary because of changes in the component fields, which is a standout advantage of the NFFF extrapolations. We notice that the α's to have an inherent upperbound ($\alpha_i \leqslant \frac{2\pi}{n}$; n is the dimension of the AR cutout), which ensures a monotonous decay of the magnetic field with height (Nakagawa & Raadu 1972). Because the field line twist depends on $\boldsymbol{B}_1$, $\boldsymbol{B}_2$ and $\boldsymbol{B}_3$ in addition to α_1 and α_2, variations in them can accommodate any extra twist that would otherwise be impossible to accommodate because of the maximal limit in α's. An example is the AR analyzed here. The two α's have attained their maximal values at which they remained fixed before and after the flares, whereas after the flare, the free energy decreases (see, Figure 10) because of readjustments of all component fields at the bottom boundary.

ORCID iDs

Prabir K. Mitra https://orcid.org/0000-0002-0341-7886
Bhuwan Joshi https://orcid.org/0000-0001-5042-2170
Avijeet Prasad https://orcid.org/0000-0003-0819-464X
Astrid M. Veronig https://orcid.org/0000-0003-2073-002X
R. Bhattacharyya https://orcid.org/0000-0003-4522-5070

References

Antiochos, S. K., DeVore, C. R., & Klimchuk, J. A. 1999, ApJ, 510, 485
Aschwanden, M. J., Boerner, P., Schrijver, C. J., & Malanushenko, A. 2013, SoPh, 283, 5
Barnes, G., Leka, K. D., Schrijver, C. J., et al. 2016, ApJ, 829, 89
Benz, A. O. 2017, LRSP, 14, 2
Bhattacharyya, R., Janaki, M. S., Dasgupta, B., & Zank, G. P. 2007, SoPh, 240, 63
Brueckner, G. E., Howard, R. A., Koomen, M. J., et al. 1995, SoPH, 162, 357
Canfield, R. C., Hudson, H. S., & McKenzie, D. E. 1999, GeoRL, 26, 627
Carmichael, H. 1964, NASSP, 50, 451
Chen, P. F. 2011, LRSP, 8, 1
Cheng, X., & Ding, M. D. 2016, ApJS, 225, 16
Cheng, X., Ding, M. D., Zhang, J., et al. 2014, ApJ, 789, 93
Cheng, X., Zhang, J., Ding, M. D., Liu, Y., & Poomvises, W. 2013, ApJ, 763, 43
Choudhary, D. P., Gosain, S., Gopalswamy, N., et al. 2013, AdSpR, 52, 1561
Clyne, J., Mininni, P., Norton, A., et al. 2007, NJPh, 9, 301
Domingo, V., Fleck, B., & Poland, A. I. 1995, SoPh, 162, 1
Fletcher, L., Dennis, B. R., Hudson, H. S., et al. 2011, SSRv, 159, 19
Forbes, T. G. 2000, JGR, 105, 23153
Forbes, T. G., Linker, J. A., Chen, J., et al. 2006, SSRv, 123, 251
Forbes, T. G., & Priest, E. R. 1984, SoPh, 94, 315
Gary, G. A., & Hagyard, M. J. 1990, SoPh, 126, 21
Gibson, S. E., & Fan, Y. 2006, JGRA, 111, A12103
Gibson, S. E., Fletcher, L., Del Zanna, G., et al. 2002, ApJ, 574, 1021
Green, L. M., Török, T., Vršnak, B., Manchester, W., & Veronig, A. 2018, SSRv, 214, 46
Hagyard, M. J., Smith, J. B., Teuber, D., et al. 1984, SoPh, 91, 115
Hannah, I. G., & Kontar, E. P. 2012, A&A, 539, A146
Hinterreiter, J., Veronig, A. M., Thalmann, J. K., Tschernitz, J., & Pötzi, W. 2018, SoPh, 293, 38
Hirayama, T. 1974, SoPh, 34, 323
Hu, Q., & Dasgupta, B. 2008, SoPh, 247, 87
Hu, Q., Dasgupta, B., Choudhary, D. P., & Büchner, J. 2008, ApJ, 679, 848
Hu, Q., Dasgupta, B., Derosa, M. L., Büchner, J., & Gary, G. A. 2010, JASTP, 72, 219
Hudson, H. S., Lemen, J. R., Cyr, O. C., St., Sterling, A. C., & Webb, D. F. 1998, GeoRL, 25, 2481
Jing, J., Tan, C., Yuan, Y., et al. 2010, ApJ, 713, 440
Joshi, B., Ibrahim, M. S., Shanmugaraju, A., & Chakrabarty, D. 2018, SoPh, 293, 107
Joshi, B., Kushwaha, U., Cho, K.-S., & Veronig, A. M. 2013, ApJ, 771, 1
Joshi, B., Kushwaha, U., Veronig, A. M., et al. 2017, ApJ, 834, 42
Joshi, B., Kushwaha, U., Veronig, A. M., & Cho, K.-S. 2016, ApJ, 832, 130
Joshi, B., Veronig, A., Manoharan, P. K., & Somov, B. V. 2012, ASSP, 33, 29
Khlystova, A., & Toriumi, S. 2017, ApJ, 839, 63
Klimchuk, J. A. 2001, GMS, 125, 143
Kopp, R. A., & Pneuman, G. W. 1976, SoPh, 50, 85
Künzel, H. 1960, AN, 285, 271
Lemen, J. R., Title, A. M., Akin, D. J., et al. 2012, SoPh, 275, 17
Liu, C., Lee, J., Yurchyshyn, V., et al. 2007, ApJ, 669, 1372
Liu, R., Liu, C., Wang, S., Deng, N., & Wang, H. 2010, ApJL, 725, L84
Liu, W., Petrosian, V., Dennis, B. R., & Jiang, Y. W. 2008, ApJ, 676, 704
Mahajan, S. M., & Yoshida, Z. 1998, PhRvL, 81, 4863
Manoharan, P. K., van Driel-Gesztelyi, L., Pick, M., & Demoulin, P. 1996, ApJL, 468, L73
Mariska, J. T. (ed.) 1992, in The Solar Transition Region (Cambridge, UK: Cambridge Univ. Press), 290
Moore, R. L., & Roumeliotis, G. 1992, in IAU Coll. 133, Eruptive Solar Flares 399, ed. Z. Svestka, B. V. Jackson, & M. E. Machado (Berlin: Springer), 69
Moore, R. L., Sterling, A. C., Hudson, H. S., & Lemen, J. R. 2001, ApJ, 552, 833
Muhamad, J., Kusano, K., Inoue, S., & Bamba, Y. 2018, ApJ, 863, 162
Nakagawa, Y., & Raadu, M. A. 1972, SoPh, 25, 127
Nindos, A., Patsourakos, S., Vourlidas, A., & Tagikas, C. 2015, ApJ, 808, 117
Patsourakos, S., Georgoulis, M. K., Vourlidas, A., et al. 2016, ApJ, 817, 14
Patsourakos, S., Vourlidas, A., & Stenborg, G. 2013, ApJ, 764, 125
Pesnell, W. D., Thompson, B. J., & Chamberlin, P. C. 2012, SoPh, 275, 3
Prasad, A., Bhattacharyya, R., Hu, Q., Kumar, S., & Nayak, S. S. 2018, ApJ, 860, 96
Priest, E. 2014, Magnetohydrodynamics of the Sun (Cambridge: Cambridge Univ. Press)
Rust, D. M., & Kumar, A. 1996, ApJL, 464, L199
Sammis, I., Tang, F., & Zirin, H. 2000, ApJ, 540, 583
Schou, J., Scherrer, P. H., Bush, R. I., et al. 2012, SoPh, 275, 229
Schrijver, C. J. 2007, ApJL, 655, L117
Sterling, A. C., Hudson, H. S., Thompson, B. J., & Zarro, D. 2000, ApJ, 532, 628
Sterling, A. C., & Moore, R. L. 2001, JGR, 106, 25227
Sturrock, P. A. 1966, Natur, 211, 695
Sun, X., Hoeksema, J.-T., Liu, Y., et al. 2012, ApJ, 748, 77
Takizawa, K., & Kitai, R. 2015, SoPh, 290, 2093
Vekstein, G. 2016, JPlPh, 82, 925820401
Veronig, A. M., Karlický, M., Vršnak, B., et al. 2006, A&A, 446, 675
Vršnak, B. 2008, AnGeo, 26, 3089
Zirin, H., & Liggett, M. A. 1987, SoPh, 113, 267
Zirin, H., & Wang, H. 1993, SoPh, 144, 37